

Infrared Small Target Detection in Satellite Videos: A New Dataset and A Novel Recurrent Feature Refinement Framework

Xinyi Ying, Li Liu, Zaiping Lin, Yangsi Shi, Yingqian Wang, Ruoqing Li, Xu Cao, Boyang Li, Shilin Zhou, Wei An

Abstract—Multi-frame infrared small target (MIRST) detection in satellite videos has been a long-standing, fundamental yet challenging task for decades, and the challenges can be summarized as follows: First, extremely small target size, highly complex clutters & noises, various satellite motions result in limited feature representation, high false alarms, and difficult motion analyses. In addition, existing methods are primarily designed for static or slightly adjusted perspectives captured by short-distance platforms, which cannot generalize well to complex background motion in satellite videos. Second, the lack of large-scale publicly available MIRST dataset in satellite videos greatly hinders the algorithm development. To address the aforementioned challenges, in this paper, we first build a large-scale dataset for MIRST detection in satellite videos (namely IRSatVideo-LEO), and then develop a recurrent feature refinement (RFR) framework as the baseline method for satellite motion estimation and compensation. Specifically, IRSatVideo-LEO is a semi-simulated dataset with synthesized satellite motion, target appearance, trajectory and intensity, which can provide a standard toolbox for satellite video generation and a reliable evaluation platform to facilitate the algorithm development. For the baseline method, RFR is proposed to be equipped with existing powerful CNN-based methods for long-term temporal dependency exploitation and integrated motion compensation & MIRST detection. Specifically, a pyramid deformable alignment (PDA) module is proposed to achieve effective feature alignment, and a temporal-spatial-frequency modulation (TSFM) module is proposed to achieve efficient feature aggregation and enhancement. Extensive experiments have been conducted to demonstrate the effectiveness and superiority of our scheme. The comparative results show that ResUNet equipped with RFR outperforms the state-of-the-art MIRST detection methods. Dataset and code are released at <https://github.com/XinyiYing/RFR>.

Index Terms—Infrared small target detection, satellite videos, recurrent network, deformable convolution.

I. INTRODUCTION

Infrared satellite surveillance is significant in diverse scenarios such as traffic monitoring [1]–[3], maritime rescue [4], [5] and early warning systems [6], [7]. Despite its valuable

X. Ying, L. Liu, Z. Lin, Y. Shi, Y. Wang, X. Cao, R. Li, S. Zhou, W. An are with the College of Electronic Science and Technology, National University of Defense Technology, P. R. China. Zaiping Lin and Wei An are the corresponding authors. Emails: yingxinyi18@nudt.edu.cn. This work was partially supported by the National Key Research and Development Program of China No. 2021YFB3100800, the National Natural Science Foundation of China under Grant 62376283, the Science and Technology Innovation Program of Hunan Province under Grant 2021RC3069, the China Postdoctoral Science Foundation under Grant Number GZB20230982, 2023M744321, and the Independent Innovation Science Fund Project of National University of Defense Technology under Grant 22-ZZCX-042.

applications, infrared satellite videos are always with strict access restrictions, resulting in data scarcity of open-source datasets. In addition, due to the technical limitations of satellite sensors, infrared satellite videos always exhibit low spatial & radiometric resolution and limited imaging quality.

Multi-frame infrared small target detection in satellite videos (MIRST-SatVideo) is a long-standing, fundamental yet challenging task in satellite surveillance systems, and has consecutively received considerable attention. Specifically, MIRST detection aims at localizing a scarce of candidate target pixels from image sequences captured by diverse earth-orbiting satellites, such as low earth-orbiting (LEO) satellites of 400-2K km, middle earth-orbiting (MEO) satellites of 2K-36K km, and geostationary earth-orbiting (GEO) satellites of 36K km. Compared toIRST detection in aerial-based and land-based imaging systems (mostly no more than 10 km),IRST detection in satellite videos remains more challenging, and has several unique characteristics.

- **Extremely small size of targets:** Due to remote sensing imaging system and optical diffraction effect, targets always appear as small points or diffraction spots, which lack geometry appearances such as contour, shape and texture.
- **Highly complex clutters and noises:** Satellite videos always contain various complex background clutters (*e.g.*, earth background clutter, stellar clutter and cloud clutter) and heavy sensor noise (*e.g.*, random thermal noise and non-uniformity device noise such as blind pixel and stripe noises). Therefore, targets usually exhibit a low signal-to-clutter ratio (SCR), and are easily immersed in various clutters and noise.
- **Various compound satellite motion:** The presence of translation, pitch, yaw, roll, jitter, and satellite scheduling significantly degrades imaging quality, leading to diminished target intensity and blurred target outlines. In addition, the coupled target and background motion pose challenges for motion information extraction and utilization. Since existing methods mainly focus on scenarios with a relatively static or slightly modified field of view, they encounter difficulties in handling the sophisticated motion characteristics of satellite video.
- **Lack of open-source datasets:** The lack of open-source MIRST datasets in satellite videos greatly hinders the advancement of MIRST detection algorithms. Therefore, a large-scale, high-quality dataset is absolutely necessary.

Dataset is the foundation underlying research development. Therefore, we build the first large-scale MIRST dataset in satellite videos (namely the IRSatVideo-LEO dataset), including 200 sequences, 91366 frames with mask annotations. Due to the limited availability of infrared satellite videos, IRSatVideo-LEO is a semi-simulated dataset with a real satellite image and synthesized satellite motion, target appearance, trajectory and intensity, which can provide a standard and efficient toolbox for satellite video generation, and offers a reliable evaluation platform to facilitate the algorithms development. Note that, in this paper, we mainly focus on LEO and GEO satellites with smoothly moving satellite platforms, while the GEO satellite videos can also be simulated by our toolbox.

Based on the IRSatVideo-LEO dataset, we develop a recurrent feature refinement (RFR) framework as the baseline method for MIRST in satellite videos. RFR can be equipped with existing deep learning-based single-frame infrared small target (SIRST) detection methods for joint satellite motion compensation and MIRST detection in a data-driven manner. Specifically, RFR employs recurrent framework [8], [9] to fully exploit the long-term temporal dependency from the entire input video. Through RFR, features are iteratively propagated and aggregated, which retains context information from all history memory to refine the current state. For feature propagation with moving platform, we employ deformable convolutions [10]–[12] to perform implicit motion compensation. Note that, considering the scale differences between background motion and target motion, we use a pyramid structure to decompose the motion, and perform target and background motion compensation in a coarse-to-fine manner. For feature aggregation, we propose a temporal-spatial-frequency modulation (TSFM) module to aggregate the beneficial temporal information from aligned features, and adaptively enhance the spatial and frequency information especially for small targets. In summary, the contributions of this paper can be summarized as follows:

- This paper, for the first time, discusses the multi-frame infrared small target detection in satellite videos (MIRST-SatVideo), and builds the first large-scale dataset (namely IRSatVideo-LEO) to lay the foundation of research development.
- Based on IRSatVideo-LEO, we develop a recurrent feature refinement (RFR) framework as a baseline method for MIRST detection in satellite videos, which can fully exploit the long-term temporal dependency to achieve satellite motion compensation and MIRST detection in an end-to-end manner.
- Extensive experiments have been conducted to demonstrate the effectiveness and superiority of our method. In addition, RFR can be easily equipped with existing SIRST detection algorithms to achieve consistent performance improvements.

This paper is organized as follows: Section II briefly reviews the related work. Section III introduces our self-developed IRSatVideo-LEO dataset in detail. Section IV introduces the architecture of our method. The experimental

results are presented in Section V. Section VI gives the conclusion.

II. RELATED WORK

In this section, we briefly review the major works of algorithms and datasets for IRST detection.

A. Algorithms for IRST Detection

IRST Detection is a long-standing, fundamental yet challenging task in infrared search and tracking systems. Due to the rapid reaction of high maneuvering target, numerous single-frame IRST detection methods have been proposed in the past decades, including early traditional paradigms (*e.g.*, filtering-based methods [13], [14], local contrast-based methods [15]–[19], low rank-based methods [20]–[24]) and recent deep learning paradigms [25]–[35].

Based on the aforementioned single-frame methods, temporal clues within sequence images can be exploited [5], [22], [36], [37] to address blur, distortion and low-contrast targets within a single frame, and can offer reasonable history tracking and future forecasting. Specifically, a variety of spatio-temporal filters (*e.g.*, 3-D matched filter [36], [38], [39], correlation filter [40], [41], particle filter [42], [43], wavelet filter [44]–[46]) are proposed to suppress low-frequency background and extract the region of interest. Recently, incorporating spatio-temporal information into local contrast-based methods [47]–[49] and low rank-based methods [5], [22], [24], [50]–[52] have raised more and more attention. Although these series of methods perform robust to low-contrast targets, their handcrafted features, fixed hyper-parameters and high computational complexity cannot generalize well to real scenes with complex background clutter and real-time application requirements. To address this problem, powerful CNN-based methods [37], [53]–[55] have emerged to learn trainable features in a data-driven manner, which can achieve state-of-the-art performance with high efficiency. Specifically, Li *et al.* designed a direction-coded convolution block to distinguish the motion between targets and clutters. Zhang *et al.* incorporated a spatial-temporal tensor (STT) optimization model into CNN-based method to achieve IRSTD in a model & data-driven manner. Yan *et al.* proposed a spatio-temporal differential multi-scale attention network (STDMANet) to extract temporal multi-scale features for IRSTD. However, these methods only focus on target motion under a relatively static field of view (some are with sudden movement by turnable collection), which cannot generalize well to the complex background motion of satellite videos.

Recently, motion estimation and compensation have been widely used in many video processing tasks, such as video super-resolution [56]–[58], video inpainting [59], [60], video object detection [2], [61], [62]. Compared with two-step optical flow-based approaches [57], [59], [61] (*i.e.*, motion estimation by optical flow approaches and frame alignment by warping) that always leads to ambiguity and duplication, deformable convolution-based methods [58], [60] achieve motion compensation in a unified step by dynamically adjusted

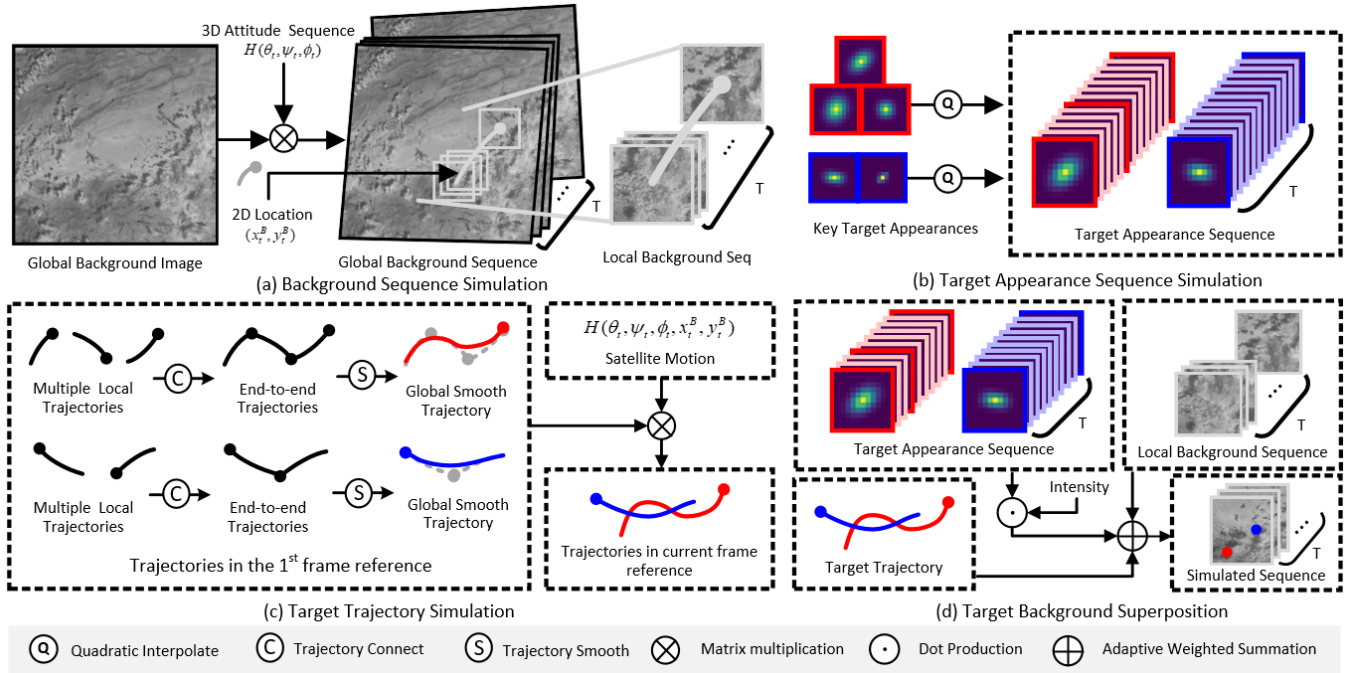


Fig. 1. Implementation details of the IRSatVideo-LEO dataset that consists of four steps: (a) Background sequence simulation. 3D attitude sequence is first used to generate a global background sequence from a SWIR satellite image by homography transformation, and 2D location is then used to crop the local background sequence. (b) Target appearance sequence simulation. Several key target appearances (e.g., red and blue Gaussian kernel images) are used to generate target appearance sequence by quadratic interpolation¹ (e.g., light red and light blue Gaussian kernel images are interpolated results). (c) Target trajectory simulation. We first generate the trajectory in the 1st frame reference by connecting and smoothing multiple separate trajectories, and then employ satellite motion to perform reference transformation to generate trajectory in the current frame reference. (d) Target background superposition. Target appearance sequence and intensity are multiplied, which is then adaptive weighted summed by background sequence using target trajectory to generate the simulated sequence.

sampling grid in a learnable manner. Therefore, we employ deformable convolution for satellite motion compensation in our paper.

B. Datasets for IRST Detection

Due to special applications [4], [22], [63], IRST datasets are always scarce. In recent decades, plenty of SIRST detection datasets [25], [26], [28], [29], [64], [65] and multi-frame IRST (MIRST) detection datasets [37], [66]–[69] have been proposed to facilitate the algorithm development.

As the pioneering open-source SIRST detection datasets, Wang *et al.* [25] synthesized 10100 images with real scenes and simulated targets. Then, Dai *et al.* [26] collected and annotated 427 images to release the first real dataset (namely SIRST), which was then extended to SIRST-v2 with 514 images [70]. To further enlarge the available dataset, the simulated NUDT-SIRST dataset and real IRSTD-1K dataset are proposed for over a thousand images. Besides the aforementioned land-based and aerial-based SIRST datasets, Wu *et al.* [65] proposed the first space-based near-infrared tiny ship dataset mounted by a low Earth-orbiting satellite.

Compared with SIRST detection datasets that only provide appearance information, consecutive frames of MIRST detection datasets allow for a more comprehensive understanding of target behavior by additional motion patterns. In addition, the inherent appearance & radiation variations, motion blur, dynamic background and various annotation forms (e.g., point,

box and mask) of MIRST detection datasets significantly increase the difficulty of this task. Hui *et al.* [66] and Fu *et al.* [67] released two real MIRST detection datasets through the 2nd and 3rd Sky Cup competitions, which contain 22 and 87 sequences with point and box annotations, respectively. Sun *et al.* [68] semi-simulated 350 image sequences (namely SIATD) with background sequences captured by UAVs and simulated target appearance and motion. SIATD only provides point annotations. Sun *et al.* [69] built a large-scale infrared small dim target dataset (IRDST). IRDST contains a real subset of 85 sequences and a simulated subset of 316 sequences with pixel-level annotations. Li *et al.* [37] synthesized a multi-frame infrared small and dim target dataset (NUDT-MIRSDT) to explore MIRST detection under extremely low signal-to-noise ratio (*i.e.*, $SNR < 3$).

Despite the valuable contributions of open-source datasets in the field of MIRST detection, these datasets are all captured by aerial-based and land-based imaging systems, and have large differences against space-based datasets (see section I for details). Due to the scarcity and unavailability of infrared satellite videos, we decide to develop the first large-scale MIRST dataset in satellite videos, namely the IRSatVideo-LEO dataset, to advance the technique development of space-based MIRST detection.

III. THE IRSATVIDEO-LEO DATASET

Large quantity, rich diversity, and high-quality labeled data are the cornerstone of deep learning-based algorithms, espe-

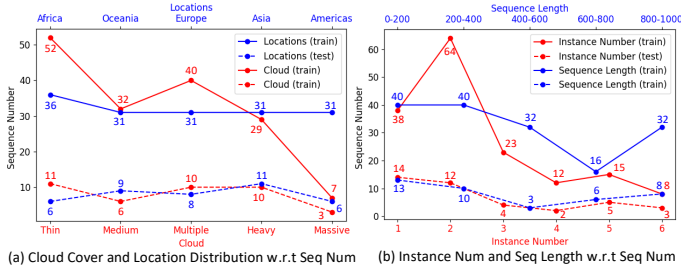


Fig. 2. Illustrations of sequence attributes. (a) shows cloud cover & location distribution with respect to (w.r.t) sequence number in training and test dataset. (b) shows instance number & sequence length with w.r.t sequence number in training and test dataset. Numbers represent the corresponding sequence number.

cially with the emergence of large-scale models. However, the inherent data scarcity of infrared satellite videos and high confidentiality of targets (*e.g.*, aircraft, missile, and launch vehicle) greatly hinder the development of MIRST detection on satellite videos. Inspired by other data-scarcity fields [68], [71]–[75], we develop a large-scale dataset (*i.e.*, IRSatVideo-LEO) using semi-simulated implementation with a real satellite image and synthesized satellite motion, target appearance, trajectory and intensity. Please refer to section III-B for more details.

A. Background Image Collection

We collect 200 background images captured by the 7th band (*i.e.*, SWIR 2.1-2.3 μm) of Landsat 8 and 9. To ensure the generalization of the dataset, we randomly sample locations across each continent and ocean on Earth, and the cloud cover ratios range from 0 to 61.25%. Figure 2 shows the cloud cover ratios and the location distributions of the IRSatVideo-LEO dataset.

B. Implementation Details

As shown in Fig. 1, to render an image sequence from a single satellite image, four steps are required: background sequence simulation, target appearance sequence simulation, target trajectory simulation and target background superposition. Then, we introduce these four steps in detail. Note that, the parameters used for data generation have been listed in Table I. Among them, different parameters result in different satellite motion, target appearance, trajectory, intensity, and thus enrich the data varieties. All parameters can adapt to accommodate more scenarios.

1) *Background Sequence Simulation*: Moving background results from satellite motion, which is composed of six degrees of freedom: 3D attitudes (*i.e.*, pitch α , yaw β , and roll γ angles) and 3D locations (*i.e.*, translation along x , y and z axes). As shown in Fig. 1 (a), we first employ the homography of 3D attitude sequence to warp the global background image to generate the global background sequence. The process can be formulated as:

$$I_t^{GB} = I^{GB} \otimes \mathbf{H}(\alpha_t, \beta_t, \gamma_t), \quad (1)$$

where $I^{GB} \in \mathbb{R}^{H_0 \times W_0}$ is the global background image, and I_t^{GB} is the global background sequence. $t \in [1, T]$ and T

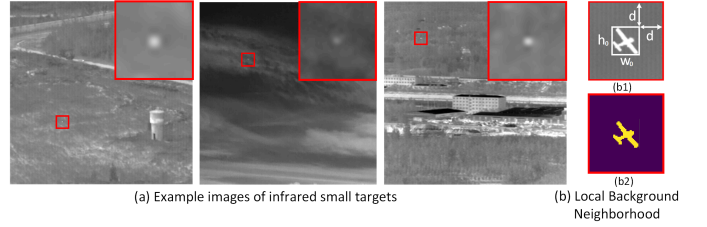


Fig. 3. Illustrations of infrared small target and local background neighborhood. (a) Example images of infrared small targets. (b1) Local background neighborhood is extended from the BBox of the target (h_0 in height and w_0 width) by d in both height and width. (b2) illustrates the target region (*i.e.*, yellow area) and local background region (*i.e.*, purple area).

is the sequence length. $\alpha_t, \beta_t, \gamma_t$ represent the pitch, yaw and roll angles at time t . $\mathbf{H}(\cdot)$ represents the homography transformation, and \otimes represents matrix multiplication. For satellite without scheduling (*i.e.*, constant attitude), we randomly set fixed 3D attitudes $(\alpha_t, \beta_t, \gamma_t) = (a, b, c)$, $a \in [-10, 10]$, $b \in [-10, 10]$, $c \in [-10, 10]$. For satellite with scheduling (*i.e.*, attitude changes slowly), we set the initial $(\alpha_1, \beta_1, \gamma_1)$ and final $(\alpha_T, \beta_T, \gamma_T)$ 3D attitudes, and employ linear interpolation to generate intermediate attitudes. Note that, scheduling range $(\Delta\alpha, \Delta\beta, \Delta\gamma) = (\alpha_T, \beta_T, \gamma_T) - (\alpha_1, \beta_1, \gamma_1)$ are randomly sampled from $[-5, 5]$, and the probability of these two modes (*i.e.*, constant attitudes, and slowly changed attitudes) are both set to 0.5.

For 3D satellite locations, translation along the z -axis is ignored due to the space-based imaging system. To generate the 2D satellite location sequence (x_t^B, y_t^B) , we randomly set the initial (x_1^B, y_1^B) and final (x_T^B, y_T^B) 2D locations, and employ quadratic interpolation¹ for intermediate locations. Note that, the velocities along x -axis and y -axis $v_x^B = \frac{x_T^B - x_1^B}{T}$, $v_y^B = \frac{y_T^B - y_1^B}{T}$ are randomly sampled from $[1/20, 2]$. Then local background sequence is cropped according to the 2D satellite location sequence, and the pre-defined field of view. The process can be formulated as:

$$I_t^{LB} = \text{Crop}(I_t^{GB}, x_t^B, y_t^B, H_0, W_0), \quad (2)$$

where $I_t^{LB} \in \mathbb{R}^{H_0 \times W_0}$ represents the local background sequence. Crop represents the crop the global background sequence I_t^{GB} by 2D satellite location x_t^B, y_t^B with a field of view of H_0, W_0 , and H_0 and W_0 in IRSatVideo-LEO are both set to 1024 [65]. Note that, our paper focuses on medium and low orbit satellites (*i.e.*, smoothly moving background), and you can set $(\alpha_t, \beta_t, \gamma_t, x_t^B, y_t^B)$ to zero or small random values for geostationary orbit satellite (*i.e.*, static or slightly jittering background). Figure 5 (a1), (b1) shows two examples of local background sequence in the 1st frame reference. It can be observed that satellite motion exhibits random, slow and smooth, which is in accordance with the real-world scenario.

2) *Target Appearance Simulation*: Due to the remote sensing imaging systems and optical diffraction effect, infrared small targets always appear as small points or

¹Given the 2D initial (x_1, y_1) and final (x_T, y_T) points, we randomly extract a segment of a low-order curve with order $p \in (0, 3)$, length $x_T - x_1$ along x -axis, and $y_T - y_1$ along y -axis.

TABLE I
 DETAILS OF PARAMETERS FOR DATA GENERATION. “BSS”, “TAS”, “TTS” AND “TBS” REPRESENT BACKGROUND SEQUENCE SIMULATION, TARGET APPEARANCE SIMULATION, TARGET TRAJECTORY SIMULATION AND TARGET BACKGROUND SUPERPOSITION.

Symbol	Description	Distribution	Value	
t	time	Linear	$t=\{1, 2, \dots, T-1, T\}$, $T \in [200, 1200]$	
α_t	Pitch angle at time t	Constant	$\alpha_t=a$, $a \in [-10, 10]$	
β_t	Yaw angle at time t	Linear	$\Delta\alpha=\alpha_T - \alpha_1$, $\Delta\alpha \in [-5, 5]$	
BSS	γ_t	Constant	$\beta_t=a$, $a \in [-10, 10]$	
		Linear	$\Delta\alpha=\beta_T - \beta_1$, $\Delta\beta \in [-5, 5]$	
		Constant	$\gamma_t=a$, $a \in [-10, 10]$	
		Linear	$\Delta\gamma=\gamma_T - \gamma_1$, $\Delta\gamma \in [-5, 5]$	
		Quadratic	$\gamma_t=a$, $a \in [-10, 10]$	
x_t^B	Translation along x-axis at time t	Quadratic	$v_x^B = (x_T^B - x_1^B)/T$, $v_x^B \in [1/20, 2]$	
y_t^B	Translation along y-axis at time t	Quadratic	$v_y^B = (y_T^B - y_1^B)/T$, $v_y^B \in [1/20, 2]$	
z_t^B	Translation along z-axis at time t	Constant	0	
H_0	Height of field of view	Constant	1024	
W_0	Width of field of view	Constant	1024	
TAS	h_t	Major axis length of Gaussian target at time t	Multiple Quadratic	$h \in [1, 9]$
	w_t	Minor axis length of Gaussian target at time t	Multiple Quadratic	$w \in [1, 9]$
	σ_t	Sigma value of Gaussian target at time t	Multiple Quadratic	$\sigma \in [0.1, 1]$
	N	Number of Gaussian targets	Constant	$N \in \{1, 2, 3, 4, 5, 6\}$
	K	Number of intermediate states of a Gaussian target	Constant	$K \in \{2, 3, 4, 5\}$
TTS	x_{nt}^T	Location x in the 1 st frame reference at time t	Multiple Smoothed Low-order Curves	-
	y_{nt}^T	Location y in the 1 st frame reference at time t	Multiple Smoothed Low-order Curves	-
	\hat{x}_{nt}^T	Location x in the current frame reference at time t	Multiple Smoothed Low-order Curves	-
	\hat{y}_{nt}^T	Location y in the current frame reference at time t	Multiple Smoothed Low-order Curves	-
	p	Order number of curve	Constant	$p \in [0, 3]$
	S	Target swerving times	Constant	$S \in \{0, 1, 2\}$
TBS	scr	SCR value of a target at time 1	Constant	$scr \in [1, 20]$
	k_{gb}	kernel size of Gaussian blur	Constant	$k_{gb} \in \{3, 5, 7\}$
	σ_{gb}	Sigma of Gaussian blur	Constant	$\sigma_{gb} \in [0.2, 0.6]$



Fig. 4. Example target trajectories in satellite videos. (a), (b), (c) shows the trajectory of target without (w/o) and with (w.) one and two swerving. Note that, discrete points of target trajectory with a sampling rate of 20 are shown for better visualization. The density of discrete points represents the velocity of the target, and dense points represent high velocity. Red arrows are specific to the swerving position.

diffraction spots. As shown in Fig. 3 (a), targets can be approximated by Gaussian kernels $G(h, w, \sigma)$ [68], [78], [79], where h , w are major & minor axis, and σ represents sigma value. We randomly simulate $N \in [1, 6]$ Gaussian targets for a image sequence, and $h \in [1, 9]$, $w \in [1, 9]$, $\sigma \in [0.1, 1]$. To generate the target appearance sequence of the n^{th} target $G_{nt}(h_t, w_t, \sigma_t)$, as shown in Fig. 1 (b), we randomly set $K \in [2, 5]$ Gaussian kernels $G_{nt_1}, G_{nt_2}, \dots, G_{nt_K}$ ($t_1=1, t_K=T, \{t_2 \dots t_{K-1}\} \in (1, T)$) as the key target appearances in a

sequence, and employ quadratic interpolation¹ to generate intermediate appearances.

3) *Target Trajectory Simulation*: Figure 4 shows some examples of target trajectories in satellite video sequences [80]. It can be observed that the real target trajectory is continuous and relatively smooth over a short time interval, which can be approximated using a low-order curve with order $p \in (0, 3)$ [68]. In addition, the target may swerve to change the moving direction and velocity. To simulate the n^{th} target trajectory with $S \in [0, 2]$ swerving times, as shown in Fig. 1 (c), we first synthetic S local target trajectories by low-order curves, and sequentially connect them end-to-end. Then, we employ 1D interpolation to smooth each intersection of two adjacent trajectories for a global smooth trajectory (x_{nt}^T, y_{nt}^T) . Figure 5 shows the trajectories of two swerved targets in the 1st frame reference. It can be observed that target trajectories are locally continuous and globally smooth, which are in accordance with the real-world target motion. It is worth noticing in Fig. 5 (b1) that, the moving direction of one target is opposite to that of the background, which indicates that the target disappears in

TABLE II

STATICAL COMPARISONS AMONG EXISTING SIRST AND MIRST DETECTION DATASETS AND OUR IRSATVIDEO-LEO DATASET. ‘‘SEQ.’’ AND ‘‘FRAME’’ REPRESENT THE NUMBER OF SEQUENCES AND FRAMES. ‘‘T-NUM.’’, ‘‘T-SIZE’’ AND ‘‘T-SCR’’ REPRESENT THE TARGET NUMBER, AVERAGE TARGET SIZE AND AVERAGE TARGET SCR, RESPECTIVELY. NOTE THAT, ‘‘T-SIZE’’ IS THE PIXEL NUMBER WITH MASK ANNOTATION, WHILE IS THE BOX AREA WITH BBOX ANNOTATION. ‘‘T-SCR’’ WITH BBOX OR POINT ANNOTATION (*) IS CALCULATED BY THE AVERAGE VALUE OF SCR AND SNR (*i.e.*, REPLACING μ_t IN EQ. 8 BY THE MAXIMUM VALUE IN TARGET REGION).

	Benchmark	Image Type	Scene Type	Label Type	Wave Band	Resolution	Seq.	Frame	T-Num.	T-Size	T-SCR
SIRST	NUST-SIRST [25]	Synthetic	Land	Mask	Thermal	129×129^1	-	10100	10337	40	5.40
	SIRST-v2 [70]	Real	Aerial	Mask	Thermal	278×366^2	-	514	648	37	12.07
	NUDT-SIRST [28]	Synthetic	Aerial/Land	Mask	Thermal	256×256	-	1327	1863	34	5.60
	IRSTD-1K [29]	Real	Land	Mask	Thermal	512×512	-	1001	1492	53	8.92
	NUDT-SIRST-Sea [65]	Real	Space	Mask	Near	998×998^3	-	5808	16929	36	15.32
MIRST	Hui [66]	Real	Land	Point	Thermal	256×256	22	16177	16944	-	5.33*
	Fu [67]	Real	Aerial	BBox	Thermal	640×480	87	21750	89174	185	4.66*
	Anti-UAV v2 [76]	Real	Land	BBox	Thermal	640×512	140	152561	152561	3219	1.32*
	IRDST-Real [69]	Real	Land	Mask	Thermal	992×742	85	40656	41801	10	6.89
	IRDST-Simulation [69]	Synthetic	Land	Mask	Thermal	720×480	316	106254	102077	6	4.68
	SIATD [68]	Synthetic	Aerial	Point	Thermal	640×512	350	150185	247080	$<7 \times 7$	6.95*
	NUDT-MIRSDT [37]	Synthetic	Aerial	Mask	Thermal	217×302^4	120	12000	11464	34	1.87
	IRSTD [77]	Real	Land	BBox	Thermal	640×512	48	50388	48565	60	10.40
	IRSatVideo-LEO	Synthetic	Space	Mask	Short Wave	1024×1024	200	91021	220126	4	6.69

¹²³⁴ Varied image resolution in NUST-SIRST dataset of $h \in [96, 327]$, $w \in [101, 442]$, SIRST-v2 dataset of $h \in [96, 1024]$, $w \in [135, 1280]$, NUDT-SIRST-Sea dataset of $h \in [740, 1024]$, $w \in [740, 1024]$, NUDT-MIRSDT dataset of $h \in [154, 324]$, $w \in [209, 407]$. The average image resolution is shown for simplicity.

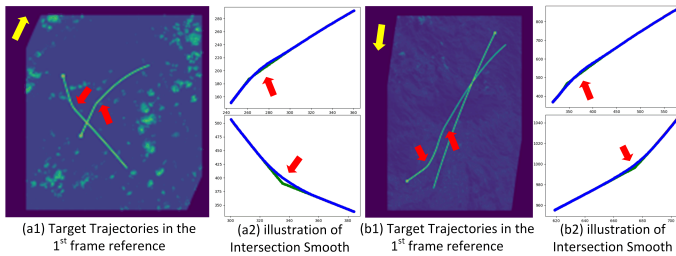


Fig. 5. Illustrations of moving background and swerving target. For moving background, (a1) and (b1) show image sets of the local background sequence in the 1st frame reference, and the yellow arrows represent the moving directions of background. For swerving target, (a1) and (b1) show the target trajectories in the 1st frame reference, and the end of trajectories are labeled by circular arrows. (a2) and (b2) show the original end-to-end adjacent trajectories (*i.e.*, green lines) and the smooth adjacent trajectories (*i.e.*, blue lines). Red arrows are specific to the swerving position.

some frames of the simulated sequence.

With satellite motion, we employ homography transformation to generate the target locations in the image plane. That is, the target trajectories in the 1st frame reference are wrapped by the homography matrix of satellite motion to generate the one in current frame reference. The process can be formulated as:

$$(\hat{x}_{nt}^T, \hat{y}_{nt}^T) = (x_{nt}^T, y_{nt}^T) \otimes \mathbf{H}(\alpha_t, \beta_t, \gamma_t, x_t^B, y_t^B), \quad (3)$$

where $(\hat{x}_{nt}^T, \hat{y}_{nt}^T)$ is the target trajectory in current frame reference, and $(\alpha_t, \beta_t, \gamma_t, x_t^B, y_t^B)$ are the parameters of satellite motion.

4) *Target Background Superposition*: As shown in Fig. 1 (d), we perform dot production between the appearance sequences G_{nt} and intensity sequences E_{nt} of the n^{th} target to generate the target template sequences I_{nt} . The formulation can be formulated as:

$$I_{nt} = G_{nt} \odot E_{nt}, \quad (4)$$

$$E_{nt} = [\text{scr} \times \sigma(T_1^{LB}) + \mu(T_1^{LB})] \times (1 + a_{nt}), \quad (5)$$

where $\mu(T_1^{LB})$ and $\sigma(T_1^{LB})$ represents the mean and standard deviation value of target local background at time 1, and scr is randomly sampled from $[1, 20]$. a_{nt} represents the target

accelerate sequence, and \odot represents element-wise multiplication. Finally, we perform adaptive weighted summation [68], [81] between the target template sequence and local background sequence, and impose a Gaussian blur function [28] for smoothness. The process can be formulated as:

$$\hat{I}_{nt}^{sim} = \text{GaussianBlur}(I_{nt}^{sim}, k_{gb}, \sigma_{gb}), \quad (6)$$

$$I_{nt}^{sim} = \text{Norm}(I_{nt}^T) \odot I_{nt}^T + (1 - \text{Norm}(I_{nt}^T)) \odot I_{nt}^{LB}, \quad (7)$$

where \hat{I}_{nt}^{sim} and I_{nt}^{LB} represent the image patch in location $(\hat{x}_{nt}^T, \hat{y}_{nt}^T)$ of simulated sequence and local background sequence, respectively. Since location $(\hat{x}_{nt}^T, \hat{y}_{nt}^T)$ is generally fractional, we follow [68], [81] to use bilinear interpolation to generate exact values. $\text{Norm}(I) = I / \max(I)$ represents image normalization, and $\max(I)$ represents the maximum value of the image. GaussianBlur represents the Gaussian blur function with kernel size $k_{gb} \in \{3, 5, 7\}$ and sigma σ_{gb} randomly sampled from $[0.2, 0.6]$.

C. Training-test Sets and Annotations

With 200 SWIR images as background images, we totally synthesize 200 video sequences. To avoid data bias and overfitting, training and test sets are split for 160 and 40 video sequences by the following criterion. 1) Each subset covers all attributes of target (*e.g.*, target number, SCR, moving speed, and swerving times, see section III-D1). 2) Each subset covers all attributes of backgrounds (*e.g.*, background complexity and moving speed, see section III-D2). 3) Two subsets are not overlapped. Figure 6 (a) shows instance number and sequence length of sequence number within training and test sets. It can be observed that instance number ranges from 1 to 6. Sequence with 2 instances occupies the largest proportion (*i.e.*, 38%), and sequence with instance number ≤ 3 is three times more than that of instance number > 3 (*i.e.*, 77.5% vs. 22.5%). In addition, sequence length ranges from 104 to 993. Among them, 26.5% are short sequences (0-200), 42.5% are medium sequences (200-600), and 31.0% are long sequences (600-1000).

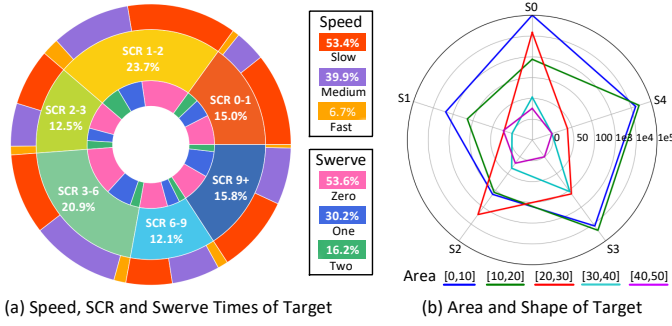


Fig. 6. Illustrations of target attributes. (a) shows speed, SCR and swerve times of targets. Middle circle shows target numbers w.r.t. target SCR, and inner and outer circles show the swerving times and target speed of different target SCR levels. Numbers in the pie chart represent the proportion of targets at each SCR level. Numbers in the legends of top-right corner and bottom-right corner represent the proportion of targets in each speed level and swerving times. (b) shows the area and shape distribution of target. “S0-S4” outside the circle represent different target shapes, of which the eccentricity range from $[0, 0.2)$, $[0.2, 0.4)$, $[0.4, 0.6)$, $[0.6, 0.8)$, $[0.8, 1]$. Lines with different colors represent different target area levels. Radius represents the annotation number, and the area under each color line represents the total annotation number of each target area level.

IRSatVideo-LEO offers two types of annotations: 1) Instance-based BBox annotations for IRST detection and tracking. 2) Instance-based mask annotation for IRST detection, semantic & instance segmentation.

D. Statistical Properties

1) *Rich Target Diversity*: We calculate the signal-to-clutter ratio (SCR), speed and swerving times of targets. Among them, SCR is calculated in the local background neighborhood of targets (see Fig. 3 (b), d is set to 20 in our paper), and can be formulated as:

$$SCR = \frac{|\mu_t - \mu_b|}{\sigma_b}, \quad (8)$$

where μ_t is the mean value of image in target region (*i.e.*, yellow area in Fig. 3 (b)). μ_b and σ_b are the mean and standard deviation values in the local background region (*i.e.*, purple area in Fig. 3 (b)). Statistical values in Fig. 6 (a) show that the number of targets with $SCR < 3$ is over a third (*i.e.*, 34.8%), which demonstrates that IRSatVideo-LEO dataset is challenging of not only small (target area $< 9 \times 9$) but also dim targets. In addition, over half of the targets present no swerve and slow speed, while a small number of targets present 1-2 swerving times (46.4%) and medium or fast speed (38.5%), enriching the target diversity and increase the difficulty of IRSatVideo-LEO dataset. In conclusion, our dataset contains high-diversity targets with different numbers, SCR, speed and swerving times, and the distribution of these attributes is controllable and in accordance with the real-world scenario. In addition, Fig. 6 (b) shows the distribution of target area, target shape w.r.t. annotation number. Since targets are simulated by Gaussian kernel, we employ eccentricity e for shape distinguishing. It can be observed that, targets smaller than 10 pixels occupy the largest proportion, and most of the targets are in circular shape.

2) *Complex Background*: Following [82], we evaluate the background complexity of a sequence by the average informa-

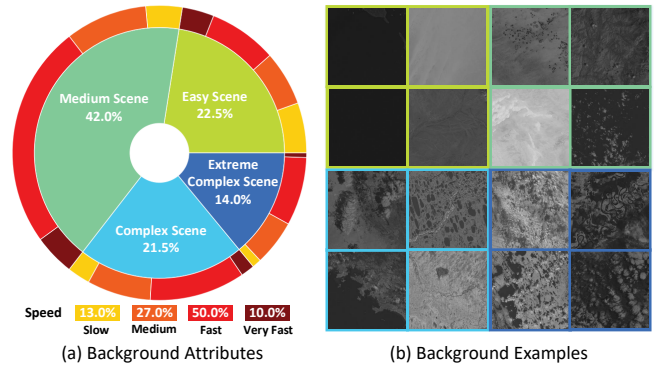


Fig. 7. Illustration of background attributes and example images. (a) shows different attributes of backgrounds. Inner circle shows background complexity w.r.t. sequence numbers, and outer circles show the background moving speed of different background complexity levels. Numbers in the pie chart represent the proportion of sequences in each background complexity. Numbers in the legends represent the proportion of sequences in each background moving speed levels. (b) shows example background images with different complexity levels.

tion entropy and variance of images in the sequence, which can be formulated as:

$$C_t = - \sum_{s=0}^{255} (s - \bar{s}(I_t)) p_s(I_t) \log(p_s(I_t)), \quad (9)$$

$$\bar{C} = \sum_{t=1}^T C_t / T, \quad (10)$$

where C_t represents the background complexity of the t^{th} frame I_t in a sequence, and \bar{C} represents the average one of the whole sequence. s represents the gray level in the histogram of I_t , and $p_s(I_t)$ is the probability of s in I_t . As shown in Fig. 7 (a), we divide background complexity into four levels: easy $\bar{C} \in [0, 200)$, medium $\bar{C} \in [200, 1000)$, complex $\bar{C} \in [1000, 2000)$ and extreme complex $\bar{C} \in [2000, \infty)$. It can be observed that our dataset covers a large range of background complexity (from 9 to 5596). In addition, we visualize some example background images in different levels in Fig. 7 (b). It can be observed that easy sequences have low background fluctuation, which increases significantly as the level increases. Moreover, we divide background moving speed (*i.e.*, average shift pixels per frame) into four levels: slow $\in [0, 1/10)$, medium $\in [1/10, 1/3)$, fast $\in [1/3, 1)$ and very fast $\in [1, 2]$. It can be observed that there exists all background moving speed levels in each background complexity level, and over 60% of sequences are in fast or even higher background moving speed. In conclusion, our dataset contains abundant backgrounds with different complexity and moving speeds.

3) *Comparison to Existing IRST Detection Datasets*: In this subsection, we make comprehensive comparisons among recent public SIRST datasets [25], [28], [29], [65], [70], MIRST datasets [66]–[69], [76] and our IRSatVideo-LEO dataset. As shown in Table II, compared to SIRST datasets, MIRST datasets are in much larger scales (*e.g.*, frame number and target number) and focus on targets with lower SCR (temporal information is necessary for MIRST detection). Note that, many MIRST datasets only provide Bounding

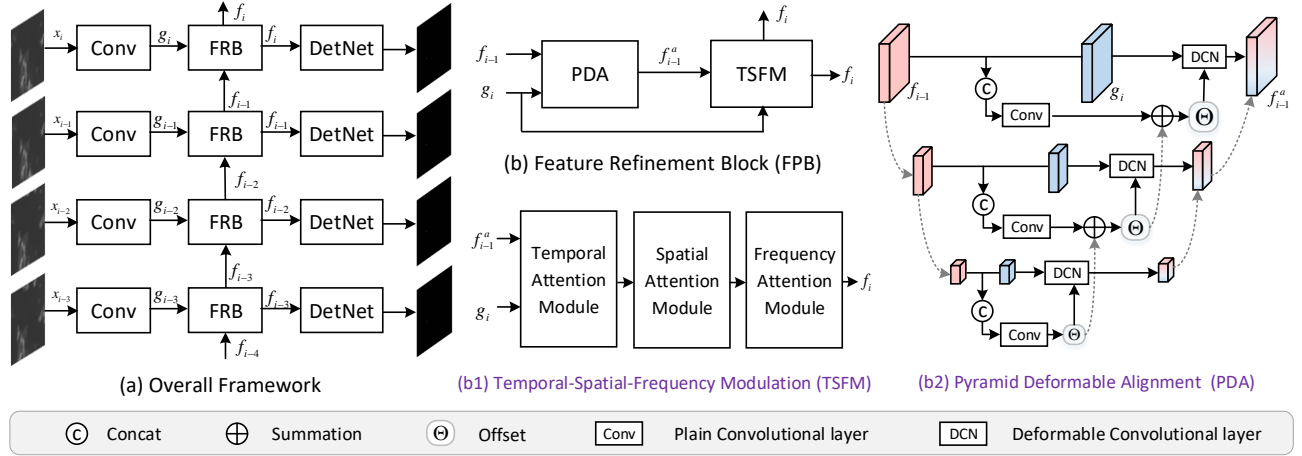


Fig. 8. The proposed architecture. (a) is the overall framework. (b) denotes feature propagation block (FRB), and (b1) and (b2) represent its submodules, including temporal-spatial-frequency modulation (TSFM) module and pyramid deformable alignment (PDA) module.

Box (BBox) or point annotations, which cannot provide a comprehensive performance evaluation among existing MIRST detection methods (*i.e.*, foreground and background segmentation task). Although IRDST and NUDT-MIRSDT datasets provide mask annotations, the land-based imaging system (*e.g.*, small field of view and disparity variations), and PTZ Camera (*e.g.*, irregular background motion results from fast and flexible platform) or static background motion cannot meet the actual conditions of satellite videos (*e.g.*, large field of view without disparity variation with respect to remote sensing imaging system, slow & regular background motion with respect to satellite cameras). In conclusion, IRSatVideo-LEO is the first large-scale MIRST dataset in satellite videos, that exhibits larger data quantity, higher image resolution, LEO satellite-based moving platform, short wave band imaging system, maneuvering small dim targets, groundtruth mask annotations, making it a valuable resource for research and development in satellite-based video surveillance and remote sensing applications.

IV. METHOD

A. Overall Framework

As shown in Fig. 8, the pipeline of our recurrent feature refinement (RFR) framework can be summarized into three components: 1) 3×3 convolution for initial feature extraction to generate initial feature $g \in \mathbb{R}^{C \times T \times H \times W}$ from the input image sequence $x \in \mathbb{R}^{1 \times T \times H \times W}$. 2) Recurrent feature refinement block (FRB) for recurrent feature alignment, propagation, aggregation and refinement. That is, FRB refines the current feature $g_i \in \mathbb{R}^{C \times H \times W}$ using recurrently refined previous features $f_{i-1} \in \mathbb{R}^{C \times H \times W}$, and thus exhibits remarkable efficiency in leveraging long-term temporal dependencies. 3) SIRST detection network for object detection. Note that, In this paper, we mainly focus on the design of recurrent FRB, which consists of a pyramid deformable alignment (PDA) module for coarse-to-fine motion compensation, and a temporal-spatial-frequency modulation (TSFM) module for multi-dimensional

information refinement. The details of PDA and TSFM are introduced in sections IV-B and IV-C.

B. Pyramid Deformable Alignment

Given the initial feature sequence $\{g_1, g_2, \dots, g_T\}$ with temporal length T , modulated deformable convolution [10], [11] is utilized to recurrently align the previous features f_{i-1} to the current features g_i , $i \in [2, T]$. Specifically, for a modulated deformable convolution with kernel size $k_h \times k_w$, the aligned feature f_{i-1}^a can be obtained by:

$$f_{i-1}^a(p_0) = \sum_{n=1}^N w(p_n) \cdot f_{i-1}(p_0 + p_n + \Delta p_n) \cdot \Delta m_n, \quad (11)$$

where p_0 denotes a location in the aligned feature. $N = k_h \times k_w$ represents the total number of the sampling locations, and p_n denotes the n^{th} value in convolutional sampling grid $G = (-\lfloor \frac{k_h}{2} \rfloor, -\lfloor \frac{k_w}{2} \rfloor), (-\lfloor \frac{k_h}{2} \rfloor, -\lfloor \frac{k_w}{2} \rfloor + 1), \dots, (\lfloor \frac{k_h}{2} \rfloor, \lfloor \frac{k_w}{2} \rfloor)$. $\lfloor \cdot \rfloor$ is the round down operation. $w(p_n)$ represents the weight in the n^{th} location of convolution kernel. Δp_n and Δm_n represent the corresponding learnable offset and learnable modulation scalar predicted by the concatenation of the previous features and the current features. The process can be defined as:

$$\Delta P_{i-1}, \Delta M_{i-1} = S(\theta([f_{i-1}, g_i])), \quad (12)$$

where $\Delta P = \{\Delta p\}$, $\Delta M = \{\Delta m\}$. $\theta(\cdot)$ represents plain convolution layers for feature embedding. $S(\cdot)$ represents channels split operation, and $[\cdot, \cdot]$ represents the concatenation operation. Following [10], [11], we employ bilinear interpolation to generate exact values since $p_0 + p_n + \Delta p_n$ is generally fractional. Compared with optical flow-based methods, deformable convolution can perform implicit motion compensation to alleviate target energy loss and outline blur caused by wrapping.

Considering the scale differences between background motion and target motion, we use a pyramid structure to decompose the motion, and perform motion compensation in a coarse-to-fine manner. Specifically, we first employ strided

TABLE III
PARAMETER SETTINGS OF 4DISTD [85], ASTTV_NTLA [22], MSLSTIPT [24], SRSTT [5], IMNN-LWEC [50], NFTDGSTV [63], AND RCTVW [86]

Method	Parameters
4DISTD [85]	Sliding step: 70, Patch size: 70×70 , $L=15$, $\lambda_1=0$, $\lambda_2=100$, $\delta_n=1/L$, $\beta_n=1e-4$, $\gamma=1e-4$, $\tau=1e-7$, $\epsilon=1e-3$
ASTTV_NTLA [22]	$L=3$, $\lambda_{tv}=0.005$, $\lambda_s = \frac{H}{\sqrt{\max(M,N)*L}}$, $H=8$, $\lambda_3=100$
MSLSTIPT [24]	$\lambda=1/\sqrt{n_3 \max(n_1, n_2)}$, $L=6$, Patch size: 30×30 , $p=0.8$
SRSTT [5]	$\lambda_1=0.05$, $\lambda_2=0.1$, $\lambda_3=100$, $\mu=0.01$, $\rho=1.3$, $\tau=1e-7$
IMNN-LWEC [50]	Sliding step: 15, Patch size: 15×15 , $L=3$, $\lambda_1 = \frac{\lambda L}{\sqrt{\max(n_1, n_2)*n_3}}$, $w: 5$, $\lambda_L=1.4$, $\lambda_2=\lambda_3=50\lambda_1$, $\epsilon=10^{-4}$, $k=1.5$, $\rho=\frac{1}{w}=\beta_{k_1 k_2}$
NFTDGSTV [63]	$L=3$, $H=4$, $\lambda_1=0.01$, $\lambda_2 = \frac{H}{\sqrt{\max(M,N)*L}}$, $\lambda_s=0.001$
RCTVW [86]	$H=4$, $\lambda = \frac{H}{\sqrt{\max(m,n)*L}}$, $\alpha=0.8$, $L=8$, $r=6$, $\beta=2e-4$, $\rho=1.1$, $\mu=0.01$

convolution filters (*i.e.*, gray down arrow with dash lines in Fig.8 (b2)) to generate L-level feature pyramids $\{f_{i-1}^l\}$ and $\{g_i^l\}$, $l \in [1, L]$ by a scale factor of 2. L is set to 3 in our paper. Within each feature pyramid level, deformable convolutions are used for feature alignment. Note that, except the lowest level L, offsets and aligned features in l^{th} level are generated by the predicted ones together with the $\times 2$ upsampled ones (*i.e.*, gray up-arrow with dash lines in Fig.8 (b2)) from the upper $(l+1)^{th}$ level. The process can be defined as:

$$\Delta P_{i-1}^l = \theta([f_{i-1}, g_i], (\Delta P_{i-1}^{l+1})^{\uparrow 2}), \quad (13)$$

$$(f_{i-1}^a)^l = \theta(\text{DCN}(f_{i-1}^l, \Delta P_{i-1}^l), ((f_{i-1}^a)^{l+1})^{\uparrow 2}), \quad (14)$$

where $(\cdot)^{\uparrow 2}$ represents bilinear upsample interpolation by a scale factor of 2. DCN represents modulated deformable convolution illustrated in Eq. 11. Note that, in the higher level of feature pyramid, we mainly focus on large-scale target motion. Subsequently, we propagate the offsets and aligned features to lower level to achieve more accurate background motion compensation. Through such a coarse-to-fine manner, sub-pixel accuracy can be obtained for precise motion compensation and target information refinement. In addition, PDA serves as a feature alignment module, and is also jointly optimized with the detection network for end-to-end training without additional supervision [83] or other pretrained models [84].

C. Temporal-Spatial-Frequency Modulation

Temporal information aggregation and target information preservation and enhancement are critical for recurrent framework. The reasons can be summarized as: 1) errors (*e.g.*, misalignment, occlusion, blurry regions, etc) are progressively accumulated and amplified through recurrent feature propagation, which significantly affect the subsequent detection performance. 2) Targets are small and feature-scarce, which are easily immersed and lost in recurrent feature propagation. Therefore, dynamic feature fusion of adjacent frames and target feature enhancement is crucial to ensuring both the effectiveness and efficiency of the recurrent feature propagation process. To handle the aforementioned problem, we propose a temporal-spatial-frequency modulation module to allocate per-pixel weight for temporal information aggregation and spatial & frequent target information enhancement. Specifically, we subsequently employ temporal

attention, spatial attention and frequent attention to fully exploit the temporal consistency, spatial saliency & frequent distinguishability of infrared small target, as shown in Fig. 8 (b1).

Temporal attention [54] aims to eliminate the misaligned, occluded, and blur pixels of aligned features for temporal feature aggregation. Specifically, we first calculate the feature similarity between the aligned feature f_{i-1}^a and the current feature g_i in an embedding space to generate the temporal attention map M_i^s . The process can be defined as:

$$M_i^s = \mathcal{P}_{Sigmoid}(\theta(f_{i-1}^a)^T \theta(g_i)), \quad (15)$$

where $\mathcal{P}_{Sigmoid}$ represents the Sigmoid function that serves as an activator to normalize the temporal attention and stabilize the training process. Awaiting of the pixel-level errors, the aligned feature is then multiplied by attention map for temporal information modulation. A plain convolutional layer is also adopted for temporal feature fusion. The process can be defined as:

$$f_i^s = \theta([f_{i-1}^a \odot M_i^s, g_i]), \quad (16)$$

where \odot is the Hadamard production.

Spatial attention [28] aims to exploit the spatial saliency prior of small target for adaptive feature enhancement. Specifically, spatial attention map is generated by the pixel-level spatial maximum and average information in an embedding space, which is then multiplied by the input feature for spatial information modulation. The process can be defined as:

$$M_i^t = \mathcal{P}_{Sigmoid}(\theta[\mathcal{P}_{max}(f_i^s), \mathcal{P}_{avg}(f_i^s)]), \quad (17)$$

$$f_i^{st} = f_i^s \odot M_i^t, \quad (18)$$

where M_i^t represents the spatial attention map. f_i^s and f_i^{st} represent the output feature of temporal and spatial information modulation. \mathcal{P}_{max} and \mathcal{P}_{avg} represent max and average operation along channel dimension, respectively.

Frequent attention [90] aims to exploit the frequent distinguishability prior of small target for enriched representation. Specifically, input feature $f_i^{st} \in \mathbb{R}^{C \times H \times W}$ is first decomposed by channels to several parts $X^i \in \mathbb{R}^{C' \times H \times W}$, $i \in \{0, 1, \dots, n-1\}$ with corresponding frequency components by 2D discrete cosine transform (DCT). $C' = C/n$. The process

TABLE IV

$P_d(\times 10^{-2})$, $F_a(\times 10^{-6})$ VALUES ACHIEVED BY DIFFERENT METHODS ON IRSATVIDEO-LEO DATASET. “#PARAMS.” REPRESENTS THE NUMBER OF PARAMETERS. FLOPS IS COMPUTED BASED ON INPUT IMAGE SEQUENCE WITH A RESOLUTION OF $20 \times 256 \times 256$, AND TIME IS COMPUTED BASED ON INPUT IMAGE SEQUENCE WITH A RESOLUTION OF $20 \times 1024 \times 1024$. THE BEST RESULTS ARE SHOWN IN RED AND THE SECOND BEST RESULTS ARE SHOWN IN BLUE.

	Methods	#Params.	FLOPs	Time	Easy			Medium			Complex			Total		
					$P_d \uparrow$	$F_a \downarrow$	AUC \uparrow	$P_d \uparrow$	$F_a \downarrow$	AUC \uparrow	$P_d \uparrow$	$F_a \downarrow$	AUC \uparrow	$P_d \uparrow$	$F_a \downarrow$	AUC \uparrow
SIRST Detection	ACM [26]	0.40M	7.40G	0.10	94.64	10.54	94.61	74.28	29.47	73.93	65.81	32.46	67.89	79.18	23.69	79.32
	ALCNet [27]	0.43M	7.50G	0.09	96.50	9.42	96.69	73.80	19.03	74.59	65.73	19.05	66.22	79.56	15.74	79.91
	DNA-Net [28]	4.69M	283.59G	6.54	79.77	1.03	80.67	46.68	5.67	46.29	61.50	8.30	64.40	60.83	4.70	61.72
	ISNet [29]	0.97M	610.08G	1.81	96.99	17.96	97.00	72.49	14.63	72.84	63.87	15.39	64.23	78.72	15.95	78.78
	UIU-Net [87]	50.54M	1087.52G	1.98	94.78	4.11	94.70	65.58	9.56	65.59	62.23	7.08	62.29	74.51	7.11	74.37
	RDIAN [69]	0.22M	74.15G	1.23	95.01	38.45	95.38	75.46	48.65	76.37	66.01	20.75	66.76	79.88	38.59	80.39
	ISTDU-Net [88]	2.75M	156.75G	1.41	97.87	12.20	97.91	76.37	19.44	76.81	67.72	16.90	70.11	81.60	16.36	82.19
	ResUNet [89]	0.91M	76.33G	0.37	96.32	20.98	96.82	72.66	20.72	73.97	65.41	14.47	68.73	78.91	19.34	80.25
	RPCANet [35]	0.68M	891.15G	3.46	97.49	23.56	97.40	71.73	20.71	71.77	65.71	17.22	65.74	78.94	20.87	78.78
	AGPCNet [34]	12.43M	863.32G	1.73	97.71	9.25	97.73	72.94	14.54	73.05	65.44	15.01	67.86	79.51	12.84	79.95
MIRST Detection	MSLSTIPT [24]	-	-	593.30	1.37	0.17	97.82	0.83	0.01	82.70	0.00	0.01	38.18	0.82	0.06	73.52
	NFTDGSTV [63]	-	-	1019.17	19.68	1.02	98.33	18.20	203.03	83.15	28.30	131.36	81.58	21.01	115.78	86.98
	RCTVW [86]	-	-	6.73	20.63	1.37	59.15	23.36	1319.96	26.16	29.17	4486.81	36.87	23.80	1732.64	39.38
	IMNN-LWEC [50]	-	-	3203.45	76.15	63.65	91.05	38.69	586.64	57.92	48.41	916.44	65.97	53.20	500.01	70.64
	SRSTT [5]	-	-	4693.61	72.01	516.64	96.01	46.73	7.07e4	58.34	39.97	2.40e5	44.63	53.46	9.28e4	65.20
	ASTTV-NTLA [22]	-	-	1148.70	88.83	8.54	90.50	63.13	106.06	66.83	73.92	71.81	79.50	73.96	64.58	77.50
	4DISTD [85]	-	-	3536.69	85.03	12.49	96.62	61.54	9.62	89.09	56.95	27.92	82.92	68.31	14.91	92.48
	STDManNet [54]	11.88M	62.98G	19.72	98.04	4.90	98.06	86.86	4.63	87.77	82.43	2.35	83.31	89.96	4.10	90.13
	DNANet_DTUM [37]	1.21M	176.66G	23.45	97.65	7.60	97.87	82.80	23.46	85.53	78.96	5.02	83.12	86.88	13.68	89.02
	ResUNet_DTUM [37]	0.30M	40.88G	3.09	99.11	33.82	99.16	87.93	76.78	89.20	81.32	12.94	83.74	90.19	47.03	91.65
	UIU-Net_DTUM [37]	51.04M	1151.19G	11.58	98.81	56.94	98.77	87.77	89.69	88.92	69.70	1107.83	70.10	87.51	318.10	87.82
	ACM_RFR	0.50M	79.88G	1.63	96.32	55.86	96.79	76.51	68.92	72.88	71.57	51.87	68.41	82.12	59.92	80.67
	ALCNet_RFR	0.53M	79.39G	1.61	97.16	13.58	97.45	77.11	7.91	78.85	70.42	4.70	72.13	82.29	9.10	83.40
	DNA-Net_RFR	4.80M	358.16G	8.05	97.77	6.21	97.97	84.13	4.15	84.60	81.67	3.95	81.90	88.11	4.81	88.36
	ISTUD-Net_RFR	2.86M	231.41G	2.89	99.22	21.22	99.23	87.23	24.36	87.91	83.14	15.87	83.80	90.31	21.29	90.68
	ResUNet_RFR	1.01M	150.90G	1.91	99.49	23.14	99.38	89.27	19.62	89.51	84.33	10.07	84.48	91.58	18.58	91.59

can be defined as:

$$\begin{aligned}
 \text{Freq}^i &= \text{DCT}^{u_i, v_i} (X^i) \\
 &= \sum_{h=0}^{H-1} \sum_{w=0}^{W-1} X_{:,h,w}^i B_{h,w}^{u_i, v_i} \\
 &\text{s.t. } , i \in \{0, 1, \dots, n-1\},
 \end{aligned} \quad (19)$$

where $\text{Freq}^i \in \mathbb{R}^{C'}$ is the frequency sub-vector, and u_i, v_i are the 2D indices of frequency components corresponding to X^i . Then, all frequency sub-vectors are concatenated to obtain the frequency vector. Afterwards, the vector is then mapped to an embedding space and activated by Sigmoid function to generate the frequent attention map. Finally, the output feature is generated by multiplication between the input feature and the frequent attention map for frequent information modulation. The process can be defined as:

$$M_i^f = \mathcal{P}_{\text{Sigmoid}}(\theta([\text{Freq}^0, \text{Freq}^1, \dots, \text{Freq}^{n-1}])), \quad (20)$$

$$f_i^{stf} = f_i^{st} \odot M_i^f, \quad (21)$$

where M_i^f represents the frequent attention map, and f_i^{stf} represents the temporal-spatial-frequent modulated feature. Note that, we employ the two-step criterion [90] to select the top-k significant frequency components.

V. EXPERIMENTS

In this section, we first introduce the experiment settings, including evaluation metrics and implemental details. Then, we apply our method to the state-of-the-art SIRST detection methods, and make comparisons with several state-of-the-art SIRST and MIRST detection methods. Finally, we present ablation studies to validate our design choice.

A. Experimental Settings

1) *Evaluation Metrics*: In this paper, we employ the probability of detection (P_d), false alarm rate (F_a), receiver operating characteristic curve (ROC), and area under curve (AUC) to evaluate the detection performance.

Probability of Detection: P_d is used to evaluate the localization capability of detection algorithms, and can be defined as:

$$P_d = \frac{\text{TD}}{\text{AT}}, \quad (22)$$

where TD and AT are the number of truly detected targets and all targets, respectively. Targets are classified as truly detected ones when their centroid deviation is lower than a pre-defined deviation threshold. Following [28], [91], we set the threshold to 3 in our paper.

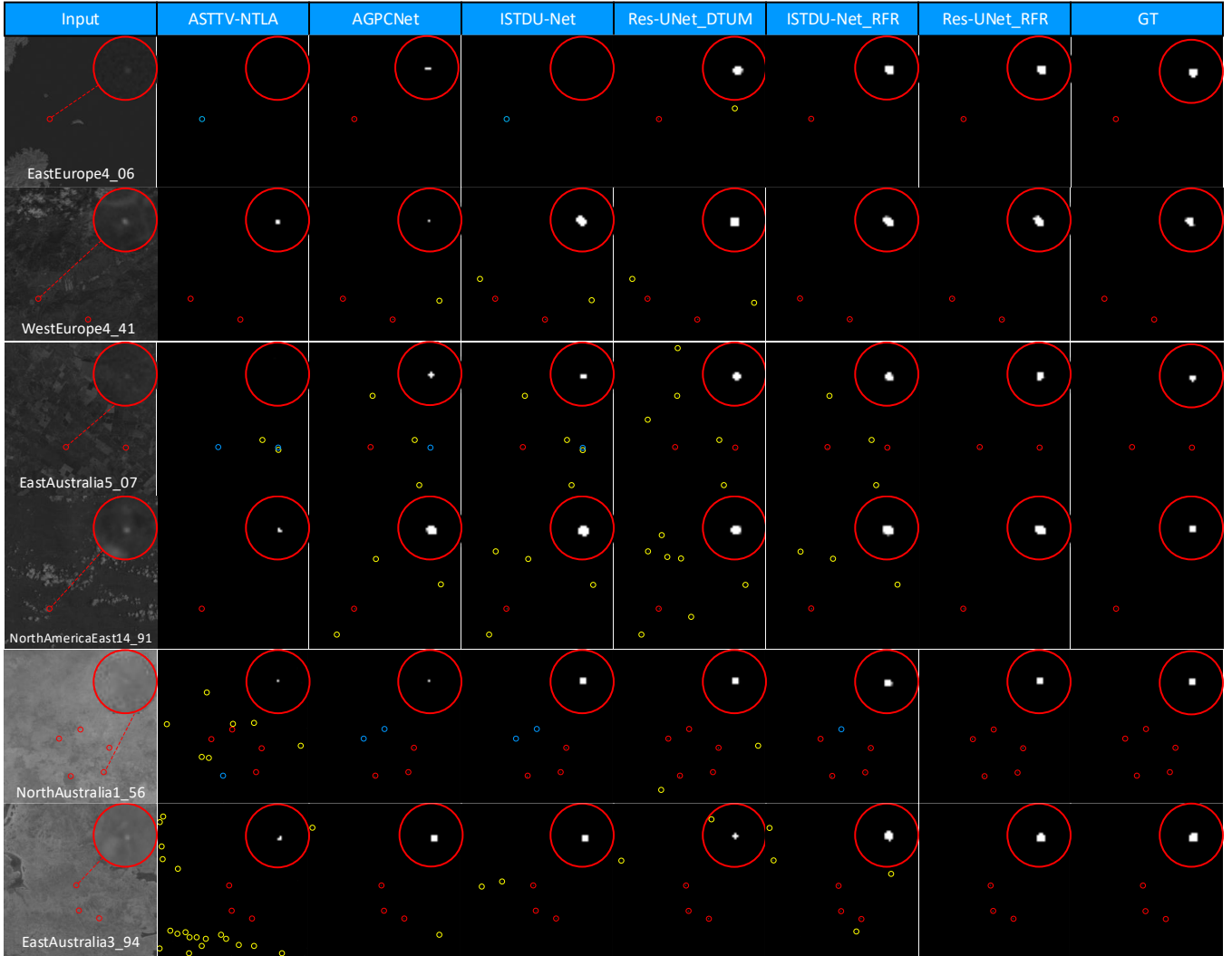


Fig. 9. Qualitative results of different methods. For better visualization, we show the zoom-in target regions on the top-right, which are highlighted by red circles. Missing detection and false alarms are highlighted by blue and yellow circles.

False Alarm Rate: F_a is used to evaluate the false alarm suppression capability of detection algorithms, and can be defined as:

$$F_a = \frac{FD}{NP}, \quad (23)$$

where FD and NP are the number of false detected pixels and all image pixels, respectively. Pixels are classified as falsely detected ones, when their centroid deviation is larger than the pre-defined deviation threshold. Following [28], [91], we set the threshold to 3 in our paper.

Receiver Operation Characteristics: ROC [28] is used to describe the trends of P_d under varying F_a .

Area Under Curve: AUC [37] is the area under ROC, and larger value represents better detection performance.

2) *Implementation Details:* During the training phase, we randomly selected K consecutive frames from all video clips in the training set of IRSatVideo-LEO, and randomly cropped a $K \times 128 \times 128$ sequence patch as the input. We followed [28], [37], [91] to augment the training data by random flipping and rotation. Note that, we control the ratio of positive samples to 0.9 to accelerate the training process. Different from the

widely used short temporal sliding window framework (mainly less than 7 input frames), our methods employ much longer sequence input (*i.e.*, $K = 10, 20, 40$ are investigated in section V-C1) for joint optimization. For test, the whole sequence is input into our recurrent feature refinement framework to capture long-term temporal dependency.

Our network was trained using the Soft-IoU loss function [28], [37] and optimized by the Adam method [92] with $\lambda_1 = 0.9$, $\lambda_2 = 0.999$. Batch size was set to 3. The learning rate was initially set to $5e-4$ and halved every 5 epochs. We trained our network from scratch for 20 epochs. All experiments were implemented in PyTorch on a PC with an Nvidia GeForce RTX 3090 GPU.

B. Comparison to the State-of-the-art Methods

In this subsection, we apply our recurrent feature refinement framework with 5 existing state-of-the-art SIRST detection methods (*i.e.*, ACM [26], ALCNet [27], DNA-Net [28], ISTDU-Net [88] and ResUNet [89]), and make comparisons to the state-of-the-art SIRST detection methods and MIRST detection methods. For SIRST detection methods, we adopt

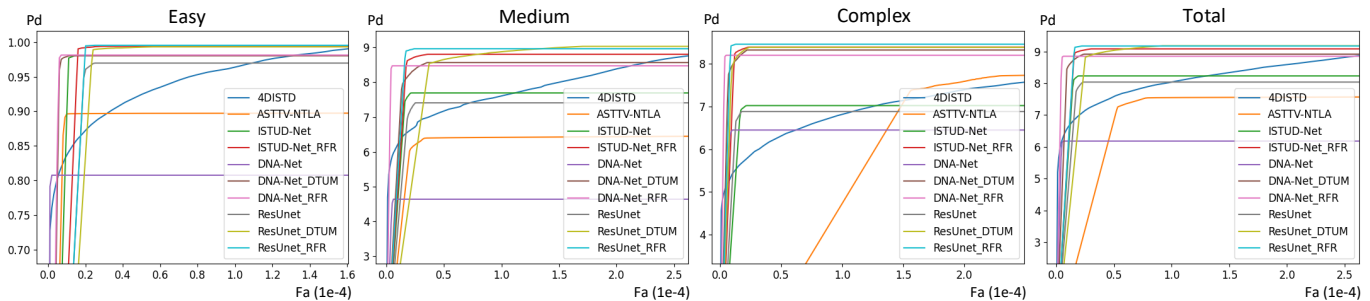


Fig. 10. ROC curves of different methods on IRSatVideo-LEO with easy scene (a), medium scene (b), complex scene (c), and all test set (d).

10 recent state-of-the-art data-driven methods (*i.e.*, ACM [26], ALCNet [27], DNA-Net [28], ISNet [29], UIU-Net [87], RDIAN [69], ISTDU-Net [88], ResUNet [89], RPCANet [35], AGPCNet [34]). For MIRST detection methods, we adopt 7 model-driven methods (*i.e.*, 4DISTD [85], ASTTV_NTLA [22], MSLSTIPT [24], SRSTT [5], IMNN-LWEC [50], NFTDGSTV [63], and RCTVW [86]) and 4 state-of-the-art data-driven methods (*i.e.*, STDMA-Net [54], DNANet+DTUM [37], ISTDUNet+DTUM [37] and ResUNet+DTUM [37]). The parameters of 7 model-driven MIRST methods are shown in Table III. For fair comparison, we retrain all the compared data-driven methods on IRSatVideo-LEO dataset from scratch under the same loss function and implemental details. Note that, the training details of SIRST detection methods are inherited from the BasicIRSTD toolbox [93], and the training details of data-driven MIRST detection methods are the same as those in section V-A2. Note that, we adopt a fixed threshold of 0.5 for all the compared algorithms.

1) *Quantitative Results*: We test different methods under three types of scenes for a more comprehensive performance evaluation. a) *Easy scene* represents the scene of target SCR higher than 6 and background complexity lower than 1000. The total number of easy scenes is 18. b) *Medium scene* represents the scene of target SCR and background complexity both higher or lower than 6 and 1000. The total number of medium scenes is 13. c) *Complex scene* represents the scene of target SCR lower than 6 and background complexity higher than 1000. The total number of complex scenes is 9.

Quantitative results are shown in Table IV. Compared with model-driven MIRST detection methods, data-driven methods introduce over 20 P_d and AUC improvements and significant suppressed false alarms, indicating the powerful modeling capability of deep learning-based methods. Compared with SIRST detection methods, MIRST detection methods introduce over 10 P_d and AUC improvements on average due to fully exploited additional temporal information. Among MIRST detection methods, ResUNet_RFR achieves the highest P_d and AUC score with reasonable false alarm increases. Note that, performance decreases as the background complexity increases and target SNR decreases. However, our methods show high robustness to complex scenes with higher P_d , AUC scores and lower F_a scores. ROC curve results are shown in Fig. 10. It can be observed that P_d of ResUNet-RFR reaches 1 faster than other compared methods, which also demonstrates the effectiveness and superiority of our method. Moreover, our RFR framework can be equipped

TABLE V
 $P_d(\times 10^2)$ AND $F_a(\times 10^6)$ VALUES ACHIEVED BY MAIN VARIANTS OF RECURRENT FRAMEWORK ON IRSATVIDEO-LEO DATASET. “-TSW $_t$ ” REPRESENTS TEMPORAL SLIDING WINDOW FRAMEWORK WITH TEMPORAL LENGTH t AND STRIDE 1. “-R $_t$ - t ” REPRESENTS RECURRENT FRAMEWORK WITH TEMPORAL LENGTH t FOR TRAINING, AND TEMPORAL SLIDING WINDOW FRAMEWORK FOR TEST WITH TEMPORAL LENGTH t AND STRIDE t . “-R $_t$ - seq ” REPRESENTS RECURRENT FRAMEWORK WITH TEMPORAL LENGTH t FOR TRAINING, AND RECURRENT FRAMEWORK FOR TEST WITH THE ENTIRE IMAGE SEQUENCE. “#PARAMS.” REPRESENTS THE NUMBER OF PARAMETERS. FLOPS IS COMPUTED BASED ON INPUT IMAGE SEQUENCE WITH SPATIAL RESOLUTION OF 256×256 AND TEMPORAL LENGTH OF t FOR “-TSW”, 20 FOR “-R”. * REPRESENTS THE FINAL MODEL. BEST RESULTS ARE SHOWN IN BOLDFACE.

Frameworks	#Params.↓	FLOPs↓	P_d ↑	F_a ↓
ResUNet	0.905M	76.325G	78.914	19.339
ResUNet-TSW $_5$	1.018M	45.200G	81.410	55.497
ResUNet-TSW $_7$	1.018M	33.956G	83.558	49.237
ResUNet-TSW $_{20}$	1.018M	11.441G	75.336	17.558
ResUNet-R $_{20-20}$	1.012M	150.895G	90.525	13.287
ResUNet-R $_{10-seq}$	1.012M	150.895G	91.025	24.802
ResUNet-R $_{20-seq}$ (*)	1.012M	150.895G	91.455	10.760
ResUNet-R $_{40-seq}$	1.012M	150.895G	91.579	18.579

with different backbones to achieve substantial performance improvements, which fully demonstrate the generalization of our method.

2) *Qualitative Results*: Qualitative results are shown in Fig. 9. It can be observed that our method outperforms all compared approaches to achieve remarkable qualitative results by accurate target localization and shape segmentation with minimal false alarms. Within the compared methods, traditional approaches present constrained capabilities in handling complex backgrounds, and often exhibit a propensity to generate a considerable number of false alarms (*e.g.*, NorthAustralia1_56 and EastAustralia3_94). In addition, ResUNet_DTUM tends to misidentify moving background clutters as targets, resulting in a substantial number of false alarms (*e.g.*, EastAustralia5_07 and NorthAmericaEast14_91). Compared with ResUNet_DTUM, ResUNet_RFR is more robust to satellite motion due to unified alignment-detection design. Moreover, as shown in lines 6-7 of Fig. 9, our RFR framework can be equipped with diverse SISRT detection techniques to achieve better performance.

3) *Computational Efficiency*: The computational efficiency (the number of parameters, FLOPs, and running time) are evaluated in Table IV. Note that, running time is the total time tested on a $20 \times 1024 \times 1024$ image sequence with an Intel(R)

TABLE VI

$P_d(\times 10^2)$ AND $F_a(\times 10^6)$ VALUES ACHIEVED BY MAIN VARIANTS OF PYRAMID DEFORMABLE ALIGNMENT ON IRSATVIDEO-LEO DATASET. “-FLOW” REPRESENTS OPTICAL FLOW-BASED METHOD FOR FEATURE ALIGNMENT. “-ATT” REPRESENTS CROSS ATTENTION MODULE FOR FEATURE ALIGNMENT. “-DA” REPRESENTS DEFORMABLE CONVOLUTION FOR FEATURE ALIGNMENT. “-PDA” REPRESENTS PYRAMID DEFORMABLE CONVOLUTION FOR FEATURE ALIGNMENT. “#PARAMS.” REPRESENTS THE NUMBER OF PARAMETERS. FLOPS IS COMPUTED BASED ON INPUT IMAGE SEQUENCE WITH A RESOLUTION OF $20 \times 256 \times 256$. (*) REPRESENTS THE FINAL MODEL. BEST RESULTS ARE SHOWN IN BOLDFACE.

Frameworks	#Params.↓	FLOPs↓	P_d ↑	F_a ↓
ResUNet w/o	0.917M	92.480G	83.149	64.886
ResUNet-Flow	0.971M	124.608G	85.715	48.197
ResUNet-Att	0.937M	105.966G	84.252	29.544
ResUNet-DA	0.939M	122.107G	90.726	13.284
ResUNet-PDA(*)	1.012M	150.895G	91.579	18.579

TABLE VII

$P_d(\times 10^2)$ AND $F_a(\times 10^6)$ VALUES ACHIEVED BY MAIN VARIANTS OF TEMPORAL-SPATIAL-FREQUENT MODULATION ON IRSATVIDEO-LEO DATASET. “-TM” REPRESENTS TEMPORAL ATTENTION FOR FEATURE MODULATION. “-TSM” REPRESENTS CASCADED TEMPORAL ATTENTION AND SPATIAL ATTENTION FOR FEATURE MODULATION. “-TSFM” REPRESENTS CASCADED TEMPORAL ATTENTION, SPATIAL ATTENTION, AND FREQUENCY ATTENTION FOR FEATURE MODULATION. “#PARAMS.” REPRESENTS THE NUMBER OF PARAMETERS. FLOPS IS COMPUTED BASED ON INPUT IMAGE SEQUENCE WITH A RESOLUTION OF $20 \times 256 \times 256$. * REPRESENTS THE FINAL MODEL. BEST RESULTS ARE SHOWN IN BOLDFACE.

Frameworks	#Params.↓	FLOPs↓	P_d ↑	F_a ↓
ResUNet w/o	1.017M	150.122G	85.243	47.224
ResUNet-TM	1.017M	150.122G	87.697	44.587
ResUNet-TSM	1.012M	150.895G	89.873	16.201
ResUNet-TSFM(*)	1.012M	150.895G	91.579	18.579

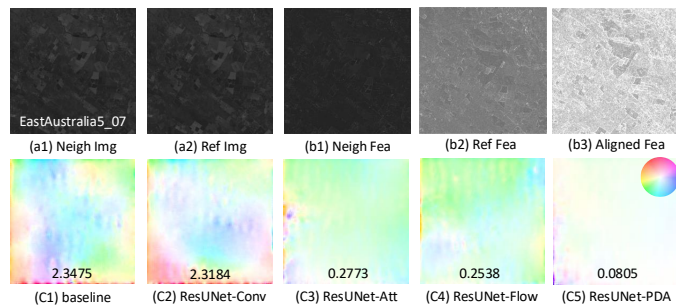


Fig. 11. Visual results of different alignment methods. (a1), (a2) show the neighborhood and reference images and (b1), (b2) show the corresponding features. (b3) shows the aligned features generated by different alignment methods, and (c2)-(c5) shows the flow (derived by RAFT [94]) between aligned and reference features of ResUNet w/o. (c1) shows the flow between neighborhood and reference features as the baseline results. Flow field color coding scheme is shown on the right. The direction and magnitude of the displacement vector are represented by hue and color intensity, respectively. Flow magnitudes are also presented within each flow.

Core(TM) i7-8700 CPU @ 3.20GHz, and is averaged over 100 runs. As compared with model-driven methods, data-driven methods achieve large-margin improvements in both detection performance and running time. Among all data-driven methods, MIRST detection methods show superior detection performance with reasonable increase in computational cost and running time.

C. Ablation Study

In this subsection, we conduct ablation experiments on our RFR framework with several variants to investigate the potential benefits introduced by our proposed modules and design choices. If not specific, ResUNet [89] is used as the baseline SIRST detection network.

1) *Recurrent Framework*: Recurrent framework performs iterative feature refinement, and thus fully exploits the long-term temporal dependency from the entire input image sequence to improve the temporal feature representation capability. To demonstrate the effectiveness of our design choice, we introduce three kinds of variants to make comparisons with widely used temporal sliding window framework, and investigate the influence of input sequence length for training and test. We also present the results of ResUNet without temporal

information exploitation as the baseline results. For fair comparison, the model sizes of all variants are set comparable, and the details of each variant are listed as follows:

- **ResUNet-TSW_t**: We employ temporal sliding window framework of temporal length t and stride 1 (t image inputs for a single image output). t is set to 5, 7, 20 in our experiments. For feature fusion, we first concatenate the input features along the channel dimension, which is then sent to several cascaded convolutional layers.
- **ResUNet-R_{t-t}**: We employ recurrent framework with temporal length t for training. For test, we employ a temporal sliding window of temporal length t and stride t (t image inputs for t image outputs), and recurrent feature refinement is within each temporal sliding window. t is set to 20 in our experiments.
- **ResUNet-R_{t-seq}**: We employ recurrent framework with temporal length t for training, and the entire image sequence is used for test. t is set to 10, 20, 40 in our experiments.

Table V shows the comparative results achieved by recurrent framework and its variants. It can be observed that improvements can be achieved among all variants against the baseline methods, which demonstrate the effectiveness of temporal additional information forIRST detection. All recurrent variants perform superior than temporal sliding window variants for 9.590 P_d and 20.402 F_a on average, which demonstrates the superiority of recurrent framework. Within the temporal sliding window variants, the detection performance increases first (*i.e.*, 2.055 gain in P_d and 5.681 drop in F_a from 5 to 7) and then decreases as the number of input frames increases (*i.e.*, 8.316 drop in P_d from 7 to 20). This is because, appropriate temporal information can introduce performance improvement, while too much temporal information with inferior fusion methods deteriorates performance instead by ambiguous and misleading information.

For recurrent variants, due to limited GPU memory and batch-based training process, temporal length of the input video clip is manually pre-defined and fixed for training. During the test phase, the whole sequence (usually contains more than 200 images, and sometimes over 900 images) can be input into the network for recurrent feature

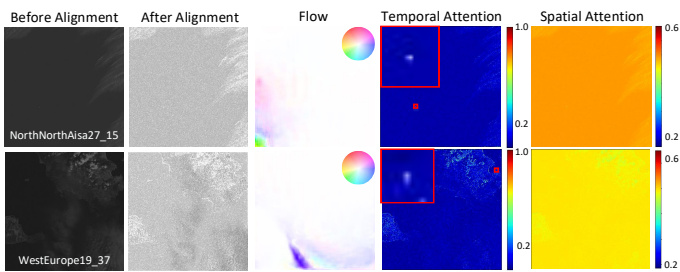


Fig. 12. Ablation on the temporal modulation (TM) and spatial modulation (SM) of TSFM. We show the temporal attention and spatial attention generated by TM and SM. Features before and after alignment, together with the flow derived by RAFT [94] are also presented. We also present the zoom-in target region for better visualization. Flow field color coding scheme is shown on the right. The direction and magnitude of the displacement vector are represented by hue and color intensity, respectively.

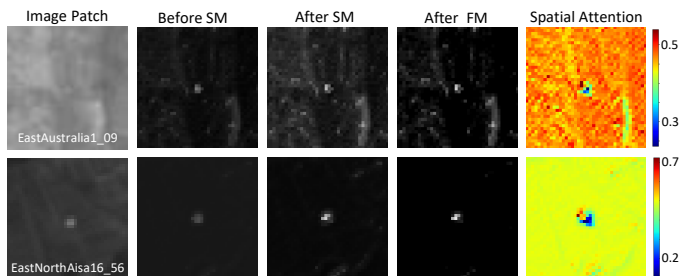


Fig. 13. Ablation on the spatial modulation (SM) and frequency modulation (FM) of TSFM. We show the zoom-in target regions of image, features before and after SM, FM. The zoom-in spatial attention is also presented.

refinement. Therefore, we investigate the influence of the input sequence length during the training and test phases. It can be observed from Table V that the performance improves steadily as the sequence length increases. This is because, recurrent frameworks effectively use the long-term temporal dependency for substantial performance improvement. Note that, as the number further increases (from 20 to 40), the improvement tends to be saturated. For a better trade-off of performance and efficiency, we employ the temporal length of 20 in the final training process. In addition, the P_d and F_a values tested on recurrent framework with fixed temporal sliding window are inferior to these on recurrent framework with entire sequence (85.726 vs. 86.468 in P_d and 19.943 vs. 18.574 in F_a), which also demonstrate the effectiveness and superiority of recurrent framework.

2) *Pyramid Deformable Alignment*: Pyramid deformable alignment is used for coarse-to-fine motion compensation specific for satellite motion. To investigate the benefits introduced by this module, we compare our PDA (*i.e.*, ResUNet-PDA) with four variants, and the details of each variant are listed as follows:

- **ResUNet w/o**: We remove PDA to test its effectiveness for feature alignment in this variant.
- **ResUNet-Flow**: We replace the deformable convolution layer in PDA by optical flow estimation using several cascaded convolution and subsequent warping for two-stage alignment in this variant.
- **ResUNet-Att**: We replace the deformable convolution layer in PDA by recent popular attention mechanism (*i.e.*,

TABLE VIII
 $P_d(\times 10^2)$ AND $F_a(\times 10^6)$ VALUES ACHIEVED BY RESUNET_RFR ON 5 IMAGE SEQUENCES WITH ONE-PIXEL TARGETS AND 5 IMAGE SEQUENCES WITH SUB-PIXEL TARGETS.

One-pixel targets		Sub-pixel targets		Total	
$P_d \uparrow$	$F_a \downarrow$	$P_d \uparrow$	$F_a \downarrow$	$P_d \uparrow$	$F_a \downarrow$
86.03	30.80	82.52	18.77	84.37	24.95

cross attention in specific) for weighted summation-based feature alignment in this variant.

- **ResUNet-DA**: We eliminate the pyramid structure in PDA by only a single deformable convolution layer for single-scale feature alignment in this variant.

Table VI shows the comparative results achieved by pyramid deformable alignment and its variants. It can be observed that deformable convolution for feature alignment is superior than optical flow-based method for 5.011 P_d gain and 34.913 F_a drop. This is because, deformable convolution employs implicit motion compensation in a unified step, avoiding ambiguous and duplicate results caused by wrapping. In addition, attention-based methods perform the worst, and even worse than flow-based methods. This is because, the complex background clutter and variable target appearance introduce much noise for spatial weighted summation operation of attention-based methods. In addition, pyramid structure can introduce 0.853 P_d gain, which further demonstrates the effectiveness of coarse-to-fine feature fusion. In Fig. 11, we show adjacent images, corresponding features, together with aligned features, and depict the flow (derived by RAFT [94]) between reference and aligned features. Compared with the flow without feature alignment, the flows of alignment modules are much smaller and cleaner. Among them, PDA achieves the smallest and cleanest flow results. It is demonstrated that PDA module can successfully compensate motions introduced by moving satellite.

3) *Temporal-Spatial-Frequent Modulation*: Temporal-spatial-frequent modulation (TSFM) is used for dynamic feature aggregation and adaptive feature enhancement. To investigate the benefits introduced by this module, we compare our TSFM with four variants, and the details of each variant are listed as follows:

- **ResUNet w/o**: We remove TSFM to test its effectiveness for temporal feature aggregation and spatial-frequency feature enhancement in this variant.
- **ResUNet-TM**: We replace TSFM by temporal modulation using temporal attention for temporal feature aggregation in this variant.
- **ResUNet-TSM**: We replace TSFM by temporal-spatial modulation using cascaded temporal attention and spatial attention for temporal feature aggregation and spatial feature enhancement in this variant.

Table VII shows the comparative results achieved by temporal-spatial-frequent modulation (TSFM) and its variants. It can be observed that temporal modulation introduces 2.454 P_d gain and 2.637 F_a drop compared with ResUNet-w/o, which demonstrates its effectiveness for feature fusion. In Fig. 12, we visualize the flow between the reference feature

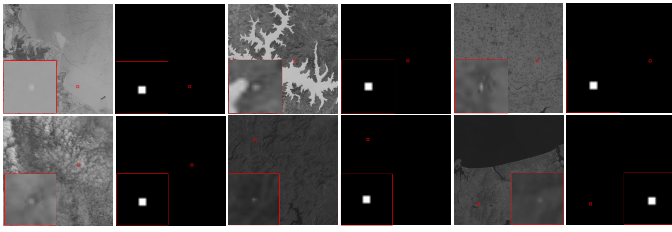


Fig. 14. Qualitative results of ResUNet_RFR method on one-pixel targets (row 1) and sub-pixel targets (row 2).

and aligned feature, together with the temporal attention map. It can be observed from the visualization of flow and temporal attention that neighborhood features can be accurately aligned, and most of the background clutters are suppressed while targets are correctly enhanced and propagated.

Spatial modulation (SM) and frequency modulation (FM) are used for feature enhancement. Ablation results in Table VII show substantial performance improvements introduced by SM and FM (2.176 and 1.706 gain for P_d). In addition, we visualize the spatial attention map, together with the features and corresponding zoom-in target region before and after SM and FM in Fig. 13. It can be observed that spatial attention and frequency attention effectively enhance the response of high-intensity and high-frequency regions, especially for small objects.

D. Discussion

In this subsection, we investigate the generalization of RFR on one-pixel targets and sub-pixel targets. Specifically, we synthesized 5 image sequences with one-pixel targets and 5 image sequences with sub-pixel targets. Based on the synthetic data, we employ ResUNet_RFR as the baseline algorithm to conduct evaluation experiments. Quantitative and qualitative results in Table VIII and Fig 14 show that ResUNet_RFR can perform robust detection on one-pixel and sub-pixel targets.

VI. CONCLUSION

In this paper, we propose a recurrent feature refinement (RFR) framework to achieve MIRST detection in satellite videos. Different from existing sliding window-based methods, RFR recurrently performs effective and efficient feature alignment, propagation, aggregation and refinement by recurrent refinement block. Specifically, pyramid deformable alignment module integrates implicit motion compensation and object detection in an end-to-end manner. Temporal spatial frequency modulation module performs dynamic feature aggregation, and exploits the spatial and frequency saliency ofIRST to preserve and enhance the target in recurrent feature propagation. Moreover, we develop an open-source MIRST dataset in satellite video to evaluate the performance of MIRST detection methods in satellite videos. Experimental results have shown the effectiveness and superiority of our method over the state-of-the-art methods.

REFERENCES

- [1] C. Xiao, T. Liu, X. Ying, Y. Wang, M. Li, L. Liu, W. An, and Z. Chen, "Incorporating deep background prior into model-based method for unsupervised moving vehicle detection in satellite videos," *IEEE Transactions on Geoscience and Remote Sensing*, vol. 61, pp. 1–14, 2023.
- [2] C. Xiao, W. An, Y. Zhang, Z. Su, M. Li, W. Sheng, M. Pietikäinen, and L. Liu, "Highly efficient and unsupervised framework for moving object detection in satellite videos," *IEEE Transactions on Pattern Analysis and Machine Intelligence*, pp. 1–8, 2024.
- [3] Q. Yin, T. Liu, Z. Lin, W. An, and Y. Guo, "Moving object detection in satellite videos via spatial-temporal tensor model and weighted Schatten p-norm minimization," *IEEE Geoscience and Remote Sensing Letters*, vol. 19, pp. 1–5, 2021.
- [4] R. Hou, P. Yan, X. Duan, and X. Wang, "Unsupervised image sequence registration and enhancement for infrared small target detection," *IEEE Transactions on Geoscience and Remote Sensing*, pp. 1–1, 2024.
- [5] J. Li, P. Zhang, L. Zhang, and Z. Zhang, "Sparse regularization-based spatial-temporal twist tensor model for infrared small target detection," *IEEE Transactions on Geoscience and Remote Sensing*, vol. 61, pp. 1–17, 2023.
- [6] Y. Zhang, Y. Zhang, R. Fu, Z. Shi, J. Zhang, D. Liu, and J. Du, "Learning nonlocal quadrature contrast for detection and recognition of infrared rotary-wing UAV targets in complex background," *IEEE Transactions on Geoscience and Remote Sensing*, vol. 60, pp. 1–19, 2022.
- [7] X. Ying, Y. Wang, L. Wang, W. Sheng, L. Liu, Z. Lin, and S. Zhou, "Local motion and contrast priors driven deep network for infrared small target super-resolution," *IEEE Journal of Selected Topics in Applied Earth Observations and Remote Sensing*, vol. 15, pp. 5480–5495, 2022.
- [8] G. Deng, Y. Ming, and J.-H. Xue, "Rfrn: A recurrent feature refinement network for accurate and efficient scene text detection," *Neurocomputing*, vol. 453, pp. 465–481, 2021.
- [9] M. Haris, G. Shakhnarovich, and N. Ukita, "Recurrent back-projection network for video super-resolution," in *IEEE conference on computer vision and pattern recognition*, 2019, pp. 3897–3906.
- [10] J. Dai, H. Qi, Y. Xiong, Y. Li, G. Zhang, H. Hu, and Y. Wei, "Deformable convolutional networks," in *IEEE International Conference on Computer Vision*, 2017, pp. 764–773.
- [11] X. Zhu, H. Hu, S. Lin, and J. Dai, "Deformable convnets v2: More deformable, better results," in *IEEE Conference on Computer Vision and Pattern Recognition*, 2019, pp. 9308–9316.
- [12] Y. Tian, Y. Zhang, Y. Fu, and C. Xu, "Tdan: Temporally-deformable alignment network for video super-resolution," in *IEEE Conference on Computer Vision and Pattern Recognition*, 2020, pp. 3360–3369.
- [13] J. Rivest and R. Fortin, "Detection of dim targets in digital infrared imagery by morphological image processing," *Optical Engineering*, vol. 35, no. 7, pp. 1886–1893, 1996.
- [14] S. D. Deshpande, M. H. Er, R. Venkateswarlu, and P. Chan, "Max-mean and max-median filters for detection of small targets," in *Signal and Data Processing of Small Targets*, vol. 3809, 1999, pp. 74–83.
- [15] C. P. Chen, H. Li, Y. Wei, T. Xia, and Y. Y. Tang, "A local contrast method for small infrared target detection," *IEEE Transactions on Geoscience and Remote Sensing*, vol. 52, no. 1, pp. 574–581, 2013.
- [16] J. Han, K. Liang, B. Zhou, X. Zhu, J. Zhao, and L. Zhao, "Infrared small target detection utilizing the multiscale relative local contrast measure," *IEEE Geoscience and Remote Sensing Letters*, vol. 15, no. 4, pp. 612–616, 2018.
- [17] S. Moradi, P. Moallem, and M. F. Sabahi, "A false-alarm aware methodology to develop robust and efficient multi-scale infrared small target detection algorithm," *Infrared Physics & Technology*, vol. 89, pp. 387–397, 2018.
- [18] J. Han, S. Moradi, I. Faramarzi, H. Zhang, Q. Zhao, X. Zhang, and N. Li, "Infrared small target detection based on the weighted strengthened local contrast measure," *IEEE Geoscience and Remote Sensing Letters*, vol. 18, no. 9, pp. 1670–1674, 2020.
- [19] J. Han, S. Moradi, I. Faramarzi, C. Liu, H. Zhang, and Q. Zhao, "A local contrast method for infrared small-target detection utilizing a tri-layer window," *IEEE Geoscience and Remote Sensing Letters*, vol. 17, no. 10, pp. 1822–1826, 2019.
- [20] Y. Dai and Y. Wu, "Reweighted infrared patch-tensor model with both nonlocal and local priors for single-frame small target detection," *IEEE Journal of Selected Topics in Applied Earth Observations and Remote Sensing*, vol. 10, no. 8, pp. 3752–3767, 2017.
- [21] L. Zhang, L. Peng, T. Zhang, S. Cao, and Z. Peng, "Infrared small target detection via non-convex rank approximation minimization joint ℓ_2 , ℓ_1 norm," *Remote Sensing*, vol. 10, no. 11, p. 1821, 2018.

- [22] T. Liu, J. Yang, B. Li, C. Xiao, Y. Sun, Y. Wang, and W. An, "Nonconvex tensor low-rank approximation for infrared small target detection," *IEEE Transactions on Geoscience and Remote Sensing*, vol. 60, pp. 1–18, 2021.
- [23] L. Zhang and Z. Peng, "Infrared small target detection based on partial sum of the tensor nuclear norm," *Remote Sensing*, vol. 11, no. 4, p. 382, 2019.
- [24] Y. Sun, J. Yang, and W. An, "Infrared dim and small target detection via multiple subspace learning and spatial-temporal patch-tensor model," *IEEE Transactions on Geoscience and Remote Sensing*, vol. 59, no. 5, pp. 3737–3752, 2020.
- [25] H. Wang, L. Zhou, and L. Wang, "Miss detection vs. false alarm: Adversarial learning for small object segmentation in infrared images," in *IEEE International Conference on Computer Vision*. IEEE, 2019, pp. 8509–8518.
- [26] Y. Dai, Y. Wu, F. Zhou, and K. Barnard, "Asymmetric contextual modulation for infrared small target detection," in *IEEE Winter Conference on Applications of Computer Vision*, 2021.
- [27] Y. Dai, Y. Wu, F. Zhou, and K. Barnard, "Attentional local contrast networks for infrared small target detection," *IEEE Transactions on Geoscience and Remote Sensing*, pp. 1–12, 2021.
- [28] B. Li, C. Xiao, L. Wang, Y. Wang, Z. Lin, M. Li, W. An, and Y. Guo, "Dense nested attention network for infrared small target detection," *IEEE Transactions on Image Processing*, vol. 32, pp. 1745–1758, 2023.
- [29] M. Zhang, R. Zhang, Y. Yang, H. Bai, J. Zhang, and J. Guo, "Isnet: Shape matters for infrared small target detection," in *IEEE Conference on Computer Vision and Pattern Recognition*, 2022, pp. 877–886.
- [30] M. Zhang, H. Bai, J. Zhang, R. Zhang, C. Wang, J. Guo, and X. Gao, "Rkformer: Runge-kutta transformer with random-connection attention for infrared small target detection," in *ACM International Conference on Multimedia*, 2022, pp. 1730–1738.
- [31] M. Zhang, K. Yue, J. Zhang, Y. Li, and X. Gao, "Exploring feature compensation and cross-level correlation for infrared small target detection," in *ACM International Conference on Multimedia*, 2022, pp. 1857–1865.
- [32] M. Ju, J. Luo, G. Liu, and H. Luo, "Istdet: An efficient end-to-end neural network for infrared small target detection," *Infrared Physics & Technology*, vol. 114, p. 103659, 2021.
- [33] Q. Hou, Z. Wang, F. Tan, Y. Zhao, H. Zheng, and W. Zhang, "Ristdnet: Robust infrared small target detection network," *IEEE Geoscience and Remote Sensing Letters*, vol. 19, pp. 1–5, 2021.
- [34] T. Zhang, L. Li, S. Cao, T. Pu, and Z. Peng, "Attention-guided pyramid context networks for detecting infrared small target under complex background," *IEEE Transactions on Aerospace and Electronic Systems*, vol. 59, no. 4, pp. 4250–4261, 2023.
- [35] F. Wu, T. Zhang, L. Li, Y. Huang, and Z. Peng, "Rpcanet: Deep unfolding rpca based infrared small target detection," in *IEEE Winter Conference on Applications of Computer Vision*, 2024, pp. 4809–4818.
- [36] I. S. Reed, R. M. Gagliardi, and H. Shao, "Application of three-dimensional filtering to moving target detection," *IEEE Transactions on Aerospace and Electronic Systems*, no. 6, pp. 898–905, 1983.
- [37] R. Li, W. An, C. Xiao, B. Li, Y. Wang, M. Li, and Y. Guo, "Direction-coded temporal u-shape module for multiframe infrared small target detection," *IEEE Transactions on Neural Networks and Learning Systems*, pp. 1–14, 2023.
- [38] I. S. Reed, R. M. Gagliardi, and L. B. Stotts, "Optical moving target detection with 3-D matched filtering," *IEEE Transactions on Aerospace and Electronic Systems*, vol. 24, no. 4, pp. 327–336, 1988.
- [39] Reed, Irving S and Gagliardi, Robert M and Stotts, Larry B, "A recursive moving-target-indication algorithm for optical image sequences," *IEEE Transactions on Aerospace and Electronic Systems*, vol. 26, no. 3, pp. 434–440, 1990.
- [40] X. Zhang, J. Ru, and C. Wu, "Infrared small target detection based on gradient correlation filtering and contrast measurement," *IEEE Transactions on Geoscience and Remote Sensing*, vol. 61, pp. 1–12, 2023.
- [41] K. Qian, H. Zhou, S. Rong, B. Wang, and K. Cheng, "Infrared dim-small target tracking via singular value decomposition and improved kernelized correlation filter," *Infrared Physics & Technology*, vol. 82, pp. 18–27, 2017.
- [42] M. Tian, Z. Chen, H. Wang, and L. Liu, "An intelligent particle filter for infrared dim small target detection and tracking," *IEEE Transactions on Aerospace and Electronic Systems*, vol. 58, no. 6, pp. 5318–5333, 2022.
- [43] J. Chen, Y. Lin, D. Huang, and J. Zhang, "Robust tracking algorithm for infrared target via correlation filter and particle filter," *Infrared Physics & Technology*, vol. 111, p. 103516, 2020.
- [44] L. Lu, "Research on infrared small target detection and tracking algorithms based on wavelet transformation," *Sensors & Transducers*, vol. 156, no. 9, p. 116, 2013.
- [45] M. A. Zaveri, S. N. Merchant, and U. B. Desai, "Wavelet-based detection and its application to tracking in an ir sequence," *IEEE Transactions on Systems, Man and Cybernetics, Part C*, vol. 37, no. 6, pp. 1269–1286, 2007.
- [46] X.-z. Su, H. Ji, and X. Gao, "Detection method for dim small ir targets based on wavelet and higher-order cumulant," in *International Symposium on Multispectral Image Processing and Pattern Recognition*, vol. 5286, 2003, pp. 911–914.
- [47] Y. Li, Y. Zhang, J.-G. Yu, Y. Tan, J. Tian, and J. Ma, "A novel spatio-temporal saliency approach for robust dim moving target detection from airborne infrared image sequences," *Information Sciences*, vol. 369, pp. 548–563, 2016.
- [48] Y. Zhao, Y. Li, C. Zhu, S. Wang, Z. Lan, and Y. Qiao, "An adaptive spatial-temporal local feature difference method for infrared small-moving target detection," in *IEEE International Conference on Network Intelligence and Digital Content*, 2023, pp. 346–351.
- [49] Y. Zhang, K. Leng, and K.-S. Park, "Infrared detection of small moving target using spatial-temporal local vector difference measure," *IEEE Geoscience and Remote Sensing Letters*, vol. 19, pp. 1–5, 2022.
- [50] Y. Luo, X. Li, S. Chen, C. Xia, and L. Zhao, "Imnn-lwec: A novel infrared small target detection based on spatial-temporal tensor model," *IEEE Transactions on Geoscience and Remote Sensing*, vol. 60, pp. 1–22, 2022.
- [51] D. Pang, P. Ma, T. Shan, W. Li, R. Tao, Y. Ma, and T. Wang, "Sttm-sfr: Spatial-temporal tensor modeling with saliency filter regularization for infrared small target detection," *IEEE Transactions on Geoscience and Remote Sensing*, vol. 60, pp. 1–18, 2022.
- [52] Y. Luo, X. Li, J. Wang, and S. Chen, "Clustering and tracking-guided infrared spatial-temporal small target detection," *IEEE Transactions on Geoscience and Remote Sensing*, pp. 1–1, 2024.
- [53] Z. Zhang, P. Gao, S. Ji, X. Wang, and P. Zhang, "Infrared small target detection combining deep spatial-temporal prior with traditional priors," *IEEE Transactions on Geoscience and Remote Sensing*, vol. 61, pp. 1–18, 2023.
- [54] P. Yan, R. Hou, X. Duan, C. Yue, X. Wang, and X. Cao, "Stdmanet: Spatio-temporal differential multiscale attention network for small moving infrared target detection," *IEEE Transactions on Geoscience and Remote Sensing*, vol. 61, pp. 1–16, 2023.
- [55] N. Zhang, Y. Liu, H. Liu, T. Tian, J. Ma, and J. Tian, "Dtnet: A specialized dual-tuning network for infrared vehicle detection in aerial images," *IEEE Transactions on Geoscience and Remote Sensing*, pp. 1–1, 2024.
- [56] T. Qing, X. Ying, Z. Sha, and J. Wu, "Video super-resolution with pyramid flow-guided deformable alignment network," in *International Conference on Electrical Engineering and Mechatronics Technology*. IEEE, 2023, pp. 758–764.
- [57] L. Wang, Y. Guo, L. Liu, Z. Lin, X. Deng, and W. An, "Deep video super-resolution using hr optical flow estimation," *IEEE Transactions on Image Processing*, vol. 29, pp. 4323–4336, 2020.
- [58] X. Ying, L. Wang, Y. Wang, W. Sheng, W. An, and Y. Guo, "Deformable 3d convolution for video super-resolution," *IEEE Signal Processing Letters*, vol. 27, pp. 1500–1504, 2020.
- [59] R. Xu, X. Li, B. Zhou, and C. C. Loy, "Deep flow-guided video inpainting," in *IEEE Conference on Computer Vision and Pattern Recognition*, 2019, pp. 3723–3732.
- [60] Z. Wu, K. Zhang, H. Xuan, J. Yang, and Y. Yan, "Dapc-net: Deformable alignment and pyramid context completion networks for video inpainting," *IEEE Signal Processing Letters*, vol. 28, pp. 1145–1149, 2021.
- [61] X. Zhu, Y. Wang, J. Dai, L. Yuan, and Y. Wei, "Flow-guided feature aggregation for video object detection," in *IEEE international conference on computer vision*, 2017, pp. 408–417.
- [62] Q. Zhou, X. Li, L. He, Y. Yang, G. Cheng, Y. Tong, L. Ma, and D. Tao, "Transvod: end-to-end video object detection with spatial-temporal transformers," *IEEE Transactions on Pattern Analysis and Machine Intelligence*, vol. 45, no. 6, pp. 7853–7869, 2022.
- [63] T. Liu, J. Yang, B. Li, Y. Wang, and W. An, "Infrared small target detection via nonconvex tensor tucker decomposition with factor prior," *IEEE Transactions on Geoscience and Remote Sensing*, 2023.
- [64] C. Gao, D. Meng, Y. Yang, Y. Wang, X. Zhou, and A. G. Hauptmann, "Infrared patch-image model for small target detection in a single image," *IEEE Transactions on Image Processing*, vol. 22, no. 12, pp. 4996–5009, 2013.

- [65] T. Wu, B. Li, Y. Luo, Y. Wang, C. Xiao, T. Liu, J. Yang, W. An, and Y. Guo, "Mtu-net: Multilevel transnet for space-based infrared tiny ship detection," *IEEE Transactions on Geoscience and Remote Sensing*, vol. 61, pp. 1–15, 2023.
- [66] B. Hui, Z. Song, H. Fan, P. Zhong, W. Hu, X. Zhang, J. Ling, H. Su, W. Jin, Y. Zhang, and Y. Bai, "A dataset for infrared detection and tracking of dim-small aircraft targets under ground / air background," *China Scientific Data*, 2020.
- [67] R. Fu, H. Fan, Y. Zhu, B. Hui, Z. Zhang, P. Zhong, D. Li, S. Zhang, G. Chen, and L. Wang, "A dataset for infrared time-sensitive target detection and tracking for air-ground application," *China Scientific Data*, 2022.
- [68] X. Sun, L. Guo, W. Zhang, Z. Wang, Y. Hou, Z. Li, and X. Teng, "A dataset for small infrared moving target detection under clutter background," *China Scientific Data*, 2021.
- [69] H. Sun, J. Bai, F. Yang, and X. Bai, "Receptive-field and direction induced attention network for infrared dim small target detection with a large-scale dataset irdst," *IEEE Transactions on Geoscience and Remote Sensing*, vol. 61, pp. 1–13, 2023.
- [70] Y. Dai, X. Li, F. Zhou, Y. Qian, Y. Chen, , and J. Yang, "One-stage cascade refinement networks for infrared small target detection," *IEEE Transactions on Geoscience and Remote Sensing*, pp. 1–17, 2023.
- [71] J. Shermeyer, T. Hossler, A. Van Etten, D. Hogan, R. Lewis, and D. Kim, "Rareplanes: Synthetic data takes flight," in *IEEE Winter Conference on Applications of Computer Vision*, 2021, pp. 207–217.
- [72] F. Zhang, X. Wang, S. Zhou, Y. Wang, and Y. Hou, "Arbitrary-oriented ship detection through center-head point extraction," *IEEE Transactions on Geoscience and Remote Sensing*, vol. 60, pp. 1–14, 2021.
- [73] C. Xiao, Q. Yin, X. Ying, R. Li, S. Wu, M. Li, L. Liu, W. An, and Z. Chen, "Dsfnet: Dynamic and static fusion network for moving object detection in satellite videos," *IEEE Geoscience and Remote Sensing Letters*, vol. 19, pp. 1–5, 2021.
- [74] Q. Yin, Q. Hu, H. Liu, F. Zhang, Y. Wang, Z. Lin, W. An, and Y. Guo, "Detecting and tracking small and dense moving objects in satellite videos: A benchmark," *IEEE Transactions on Geoscience and Remote Sensing*, vol. 60, pp. 1–18, 2021.
- [75] X. Ying, C. Xiao, R. Li, X. He, B. Li, Z. Li, Y. Wang, M. Hu, Q. Xu, Z. Lin, M. Li, S. Zhou, W. An, W. Sheng, and L. Liu, "Visible-thermal tiny object detection: A benchmark dataset and baselines," *arXiv preprint arXiv:2406.14482*, 6 2024.
- [76] N. Jiang, K. Wang, X. Peng, X. Yu, Q. Wang, J. Xing, G. Li, Q. Ye, J. Jiao, Z. Han *et al.*, "Anti-uav: a large-scale benchmark for vision-based uav tracking," *IEEE Transactions on Multimedia*, 2021.
- [77] X. Tong, Z. Zuo, S. Su, J. Wei, X. Sun, P. Wu, and Z. Zhao, "St-trans: Spatial-temporal transformer for infrared small target detection in sequential images," *IEEE Transactions on Geoscience and Remote Sensing*, vol. 62, pp. 1–19, 2024. [Online]. Available: <https://github.com/aurora-sea/SIRSTD>
- [78] S. Kim and J. Lee, "Scale invariant small target detection by optimizing signal-to-clutter ratio in heterogeneous background for infrared search and track," *Pattern Recognition*, vol. 45, no. 1, pp. 393–406, 2012.
- [79] H. Zhang, L. Zhang, D. Yuan, and H. Chen, "Infrared small target detection based on local intensity and gradient properties," *Infrared Physics & Technology*, vol. 89, pp. 88–96, 2018.
- [80] Q. Yin, Q. Hu, H. Liu, F. Zhang, Y. Wang, Z. Lin, W. An, and Y. Guo, "Detecting and tracking small and dense moving objects in satellite videos: A benchmark," *IEEE Transactions on Geoscience and Remote Sensing*, 2021.
- [81] S. Kim and J. Lee, "Scale invariant small target detection by optimizing signal-to-clutter ratio in heterogeneous background for infrared search and track," *Pattern Recognition*, vol. 45, no. 1, pp. 393–406, 2012.
- [82] H. Wang, M. Feng-Hua, C. Guo-Jun, and D. Xi-Wen, "An evaluation criterion of infrared image complexity based on background optimal filter scale," *Acta Physica Sinica*, vol. 64, no. 23, 2015.
- [83] W. Zhu and Y. Tan, "A moving infrared small target detection method based on optical flow-guided neural networks," in *International Conference on Computer Vision, Image and Deep Learning*. IEEE, 2023.
- [84] Y. Luo, X. Ying, R. Li, Y. Wan, B. Hu, and Q. Ling, "Multi-scale optical flow estimation for video infrared small target detection," in *International Conference on Computer Science, Electronic Information Engineering and Intelligent Control Technology*. IEEE, 2022.
- [85] F. Wu, H. Yu, A. Liu, J. Luo, and Z. Peng, "Infrared small target detection using spatiotemporal 4-d tensor train and ring unfolding," *IEEE Transactions on Geoscience and Remote Sensing*, vol. 61, pp. 1–22, 2023.
- [86] T. Liu, J. Yang, B. Li, Y. Wang, and W. An, "Representative coefficient total variation for efficient infrared small target detection," *IEEE Transactions on Geoscience and Remote Sensing*, 2023.
- [87] X. Wu, D. Hong, and J. Chanussot, "Uiu-net: U-net in u-net for infrared small object detection," *IEEE Transactions on Image Processing*, vol. 32, pp. 364–376, 2022.
- [88] Q. Hou, L. Zhang, F. Tan, Y. Xi, H. Zheng, and N. Li, "Istdu-net: Infrared small-target detection u-net," *IEEE Geoscience and Remote Sensing Letters*, vol. 19, pp. 1–5, 2022.
- [89] X. Xiao, S. Lian, Z. Luo, and S. Li, "Weighted res-unet for high-quality retina vessel segmentation," in *International Conference on Information Technology in Medicine and Education*. IEEE, 2018.
- [90] Z. Qin, P. Zhang, F. Wu, and X. Li, "Fcanet: Frequency channel attention networks," in *IEEE International Conference on Computer Vision*, 2021, pp. 783–792.
- [91] X. Ying, L. Liu, Y. Wang, R. Li, N. Chen, Z. Lin, W. Sheng, and S. Zhou, "Mapping degeneration meets label evolution: Learning infrared small target detection with single point supervision," in *IEEE Conference on Computer Vision and Pattern Recognition*, 2023, pp. 15 528–15 538.
- [92] D. P. Kingma and J. Ba, "Adam: A method for stochastic optimization," in *International Conference on Learning Representations*, 2015.
- [93] "Basicirstd," 2022. [Online]. Available: <https://github.com/XinyiYing/BasicIRSTD>
- [94] Z. Teed and J. Deng, "Raft: Recurrent all-pairs field transforms for optical flow," in *European Conference on Computer Vision*, 2020, pp. 402–419.



Xinyi Ying received the M.E. degree in information and communication engineering from National University of Defense Technology (NUDT), Changsha, China, in 2021. She is currently pursuing the Ph.D. degree with the College of Electronic Science and Technology, NUDT. Her research interests focus on detection and tracking of infrared small targets.



Li Liu received the Ph.D. degree in information and communication engineering from the National University of Defense Technology (NUDT), China, in 2012. From 2008 to 2010, she worked as a Visiting Student at the University of Waterloo, Canada, advised by Professor Paul Fieguth. From 2015 to 2016, she spent ten months visiting the Multimedia Laboratory at the Chinese University of Hong Kong, working with Professor Xiaogang Wang. From 2016.12 to 2018.9, she worked as a senior researcher at CMVS of the University of Oulu, Finland, working with Professor Matti Pietikainen. She was a cochair of nine International Workshops at CVPR, ICCV, and ECCV. She served as guest editor for two special issues in IEEE TPAMI and one in IJCV. She serves as an Associate Editor for IEEE Transactions on Circuits and Systems for Video Technology, IEEE Transactions on Geoscience and Remote Sensing and Pattern Recognition. She has been rated as one of the Most Cited Researchers in China. Her current research interests include Computer Vision, Machine Learning, Artificial Intelligence, Trustworthy AI, Synthetic Aperture Radar Imagery Analysis. Her papers have currently over 14,000 citations in Google Scholar (Until 2024.6.20). Her recent survey paper titled Deep Learning for Generic Object Detection.



Zaiping Lin received the B.Eng. and Ph.D. degrees from the National University of Defense Technology (NUDT), Changsha, China, in 2007 and 2012, respectively. He is currently an Associate Professor with the College of Electronic Science and Technology, NUDT. His research interests include infrared image processing and signal processing



Yangsi Shi received his B.E. degree in Communication Engineering from Sun Yat-sen University, Shenzhen, China, in 2023. He is currently pursuing his M.E. degree in Information and Communication Engineering at the National University of Defense Technology (NUDT), Changsha, China. His research interests include target detection, with a particular focus on infrared small and weak target detection.



Shilin Zhou is currently a Professor with the College of Electronic Science and Technology, National University of Defense Technology, China. His main research interests include pattern recognition, signal processing, computer vision, intelligent information processing, and remote sensing image processing.



Yingqian Wang received his B.E. degree in electrical engineering from Shandong University, Jinan, China, in 2016, the Master and the Ph.D. degrees in information and communication engineering from National University of Defense Technology (NUDT), Changsha, China, in 2018 and 2023, respectively. Dr. Wang is currently an assistant professor with the College of Electronic Science and Technology, NUDT. His research interests focus on light field image processing, image super-resolution and infrared small target

detection.



Ruoqing Li received the B.E. degree in electronic engineering from the National University of Defense Technology (NUDT), Changsha, China, in 2020, where she is currently pursuing the Ph.D. degree in information and communication engineering. Her research interests include infrared small target detection, particularly on multiframe detection and deep learning.



Xu Cao received the B.E. degree in information engineering in 2018, and the M.E. degree in information and communication engineering from National University of Defense Technology (NUDT), Changsha, China, in 2021. He is currently pursuing the Ph.D. degree with the College of Electronic Science and Technology, NUDT. His research interests focus on object detection and multi-source information fusion interpretation.



Wei An received the Ph.D. degree from the National University of Defense Technology (NUDT), Changsha, China, in 1999. She was a Senior Visiting Scholar with the University of Southampton, Southampton, U.K., in 2016. She is currently a Professor with the College of Electronic Science and Technology, NUDT. She has authored or co-authored over 100 journal and conference publications. Her current research interests include signal processing and image processing.



Boyang Li received the Ph.D and Master degrees from NUDT and National Defense Technology Innovation Institute in 2024 and 2020, respectively. Before that, He received the B.E. degree from Tianjin University in 2017. Currently, he is an assistant professor with the College of Electronic Science and Technology, NUDT. His research interests focus on optical image processing, interpretation and application, particularly on infrared small target detection, weakly supervised semantic segmentation, and neural

network compression and acceleration.